

Supporting Information

Magnetic Semiconductor Gd-Doping CuS Nanoparticles as Activatable Nanoprobes for Bimodal Imaging and Targeted Photothermal Therapy of Gastric Tumors

Hua Shi,^{£,†} Yidan Sun,^{£,‡} Runqi Yan,^{£,‡} Shunli Liu,[†] Li Zhu,[†] Song Liu,[†] Yuzhang Feng,[§]

Peng Wang,[§] Jian He,^{*,†} Zhengyang Zhou,^{*,†} and Deju Ye^{*,‡}

[†] Department of Radiology, Nanjing Drum Tower Hospital, the Affiliated Hospital of Nanjing University Medical School, Nanjing, 210008, China

[‡] State Key Laboratory of Analytical Chemistry for Life Science, School of Chemistry and Chemical Engineering, Nanjing University, Nanjing, 210093, China

[§] National Laboratory of Solid State Microstructures, College of Engineering and Applied Sciences and Collaborative Innovation Center of Advanced Microstructures, Nanjing University, Nanjing, 210093, China

[£] These authors contributed equally

* Corresponding authors:

(J.H.) E-mail: hjxueren@126.com. Phone number: +862583597518

(Z.Z.) E-mail: zyzhou@nju.edu.cn. Phone number: +862583597518

(D.Y.) E-mail: dejuye@nju.edu.cn. Phone number: +862589681905

Table of Contents

Table of Contents

		Page
1	General materials and Methods	S3
2	Synthesis of (QSY21)-GGPLGVRGK(Cy5.5)-SS and Scheme S1	S4-5
3	Synthesis of OA-coated Gd/CuS nanodisks, T-MAN and T-MAN-ctrl	S6-7
4	General procedure for the detection of MMP-2 with T-MAN	S7
5	Enzyme kinetic studies of T-MAN towards MMP-2	S7-8
6	Determination of sensitivity and specific towards MMP-2	S8
7	Measurement of longitudinal r_1 relaxivity	S8-9
8	Evaluation of photothermal effect <i>in vitro</i> .	S9
9	Cell culture	S9
10	Western blotting analysis of MMP-2 and $\alpha_v\beta_3$ integrin expression	S9-10
11	FL imaging of MMP-2 activity in MKN45 tumor cells and GES-1 normal gastric cells.	S10
12	Colocalization studies	S10
13	<i>In vitro</i> cytotoxicity induced by PTT	S10-11
14	Fluorescence imaging with Calcein AM/PI staining	S11
15	Animals and tumor models	S11-12
16	Fluorescence imaging of MMP-2 in mice	S13
17	Noninvasive MR imaging of tumors in mice	S13-14
18	Bioluminescence imaging of the orthotopic gastric tumors	S14
19	Fluorescence imaging of tissue slices	S14-15
20	<i>In Vivo</i> PTT of tumor and LN Metastasis	S15-16
21	Biodistribution studies	S16
22	Histopathological analysis	S16-17
23	Statistical analysis	S17
24	Figure S1-38	S18-37
25	Table S1-2	S38
26	Note S1-S3	S39-43
27	References	S44-45

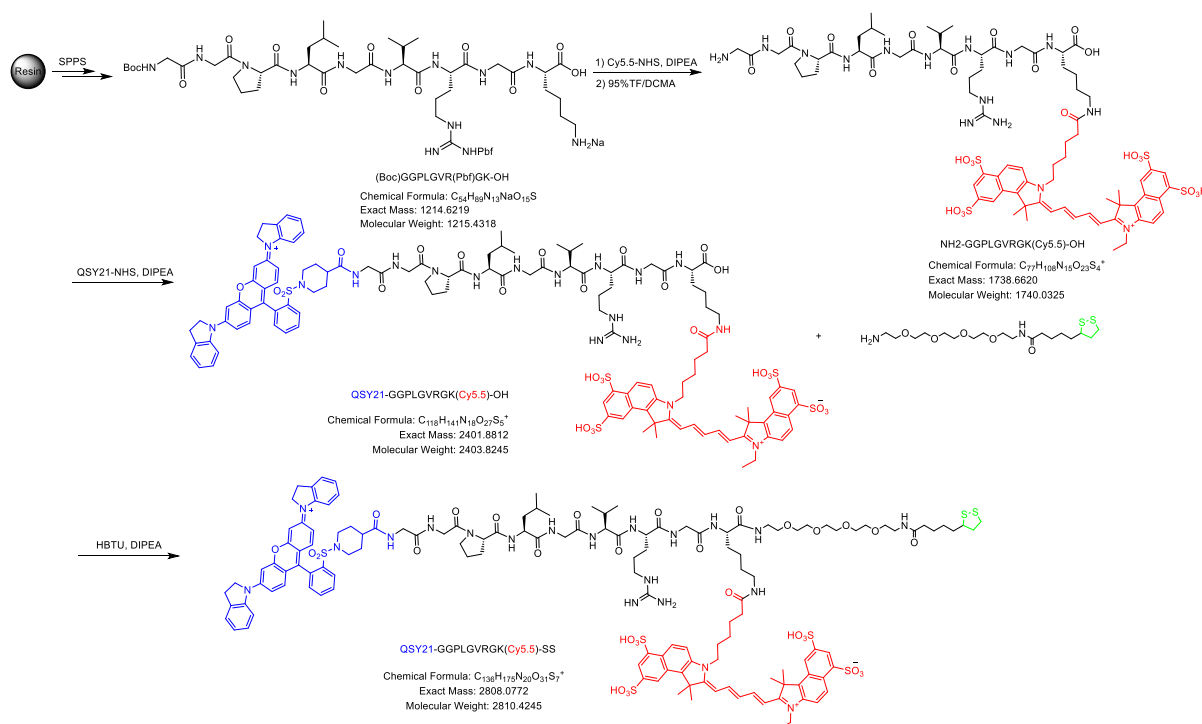
Experimental Section

General materials. All chemicals and biological reagents were purchased from commercial suppliers and used without further purification. CuCl_2 was purchased from J&K Scientific Ltd (Shanghai, China). $\text{GdCl}_3 \cdot 6\text{H}_2\text{O}$ was purchased from Sigma-Aldrich, Inc. (America). Oleyamine (OLA) and cyclohexane were purchased from Adamas-beta (Shanghai, China). Sulfur powder was purchased from Xiya Reagent (Shandong, China). DSPE-PEG₂₀₀₀-OMe and DSPE-PEG₂₀₀₀-NH₂ were purchased from Shanghai Ponsure Biotech, Inc (Shanghai, China). cRGD-SH was purchased from GL Biochem Ltd (Shanghai, China). Matrix metalloproteinase-2 (MMP-2) and SB-3CT were obtained from R&D Systems (America). Calcein AM, propidium iodide (PI), Lyso-Tracker Green, and Hoechst 33342 was obtained from KeyGen Biotech. Co. Ltd. (Nanjing, China).

Methods. Transmission electron microscopic (TEM) images were acquired with a JEM-2800 transmission electron microscope (JEOL, Ltd., Japan). HRTEM and elemental mapping images were acquired with a TECNAI F20 transmission electron microscope (FEI, America). X-ray powder diffraction (XRD) patterns were obtained on a Bruker D8 advance spectrometer (Bruker AXS Inc., America). The X-ray photoelectron spectra (XPS) were recorded using a PHI 5000 VersaProbe system (ULVAC-PHI, Inc., Japan) employing monochromatic Al $K\alpha$ as the X-ray resource. Inductively coupled plasma mass spectrometry (ICP-MS) analysis were acquired with a Optima 5300DV plasma spectrum mass spectrometer (PE, America). The number of synthesized nanoparticles was acquired by using the instrument of ViewSizer® 3000 (MANTA Instrument, Inc. America). Dynamic light scattering (DLS) and zeta potential analysis were measured by 90 Plus/BI-MAS equipment (Brookhaven, America). The fluorescence spectra were measured with a HORIBA Instruments Incorporated Fluomax-4 spectrofluorometer. The UV-vis spectra were measured with an Ocean Optics Maya 2000 Pro spectrometer. High performance liquid chromatography (HPLC) was carried out on Thermo Scientific Dionex Ultimate 3000. High-resolution Matrix-Assisted Laser Desorption/Ionization

Time of Flight Mass Spectrometry (MALDI-MS) was conducted on AB SCIEX 4800 Plus MALDI TOF/TOFTM mass spectrometer. Fluorescence images were acquired on an Olympus IX73 fluorescent inverted microscope (Olympus, Japan). Whole-body fluorescence images were acquired using an IVIS Lumina XR III system (excitation, 660 nm; emission, 710 nm). The *in vivo* MR imaging experiments were performed on a 1.0 T small animal MRI system (Bruker ICON).

Synthesis of (QSY21)-GGPLGVRGK(Cy5.5)-SS



Scheme S1. Synthesis of (QSY21)-GGPLGVRGK(Cy5.5)-SS.

Synthesis of (Boc)GGPLGVR(Pbf)GK-OH. (Boc)GGPLGVR(Pbf)GK-OH was synthesized manually on 2-Chlorotrityl Chloride Resin by a standard Fmoc-based solid-phase peptide synthesis protocol. The crude peptide product was precipitated by the addition of diethyl ether and purified by preparative HPLC (221 mg, yield 92 %). The product was characterized by high-resolution MALDI-MS (Figure S35), calcd. For C₅₄H₉₀N₁₃O₁₅S⁺ [M + H]⁺: 1192.6400 and C₅₄H₈₉N₁₃NaO₁₅S⁺ [M+Na]⁺: 1412.6219; found: 1192.5153 and 1412.4974.

Synthesis of NH₂-GGPLGVRGK(Cy5.5)-OH. A mixture of (Boc)GGPLGVR(Pbf)GK-OH (3.87 mg, 3.25 nmol), Cy5.5 NHS ester (5.49 mg, 4.86 nmol) and *N,N*-diisopropylethylamine (DIPEA, 1.69 μ L, 9.75 nmol) in anhydrous dimethylformamide (DMF, 500 μ L) was kept stirring at room temperature (r.t.) for 2 h. The crude product was precipitated by the addition of the reaction mixture into cold diethyl ether. After centrifugation, the blue precipitate was vigorously stirring in a solution containing trifluoroacetic acid (TFA) and dichloromethane (DCM) (95/5, v/v, 2 mL) at r.t. for 3 h to remove the protecting groups of Boc and Pbf. The solution was then removed under vacuum, and the residue was purified by preparative HPLC to afford NH₂-GGPLGVRGK(Cy5.5)-OH as a blue powder after lyophilization (4.3 mg, yield 76 %). The product was characterized by high-resolution MALDI-MS (Figure S36), calcd. For C₇₇H₁₀₈N₁₅O₂₃S₄⁺ [M]⁺: 1738.6620; found: 1738.4682.

Synthesis of QSY21-GGPLGVRGK(Cy5.5)-OH. A mixture of NH₂-GGPLGVRGK(Cy5.5)-OH (2.18 mg, 1.25 nmol), QSY21 NHS ester (1.23 mg, 1.5 nmol) and DIPEA (2.2 μ L, 12.5 nmol) in anhydrous DMF (500 μ L) was stirring at r.t. for 2 h. After reaction, the mixture was purified by preparative HPLC to afford QSY21-GGPLGVRGK(Cy5.5)-OH as a blue powder after lyophilization (2.4 mg, yield 80 %). The product was characterized by high-resolution MALDI-MS (Figure S37), calcd. for C₁₁₈H₁₄₁N₁₈O₂₇S₅⁺ [M]⁺: 2401.8812; found: 2402.2333.

Synthesis of (QSY21)-GGPLGVRGK(Cy5.5)-SS. To a solution of QSY21-GGPLGVRGK(Cy5.5)-OH (2.4 mg, 0.99 nmol), (2-(1*H*-benzotriazol-1-yl)-1,1,3,3-tetramethyluronium hexafluorophosphate (HBTU, 1.89 mg, 4.99 nmol) and DIPEA (0.9 μ L, 4.99 nmol) in anhydrous DMF (1 mL), amido-PEG₄-dithiolane (2.12 mg, 4.99 nmol) were added. The reaction mixture was stirring at r.t. for 6 h. After reaction, the mixture was purified by preparative HPLC to afford (QSY21)-GGPLGVRGK(Cy5.5)-SS as a blue powder after lyophilization (1.5 mg, yield 53 %). The product was characterized by high-resolution MALDI-MS (Figure S38, calcd for C₁₃₆H₁₇₅N₂₀O₃₁S₇⁺ [M]⁺: 2808.0772; found: 2808.9642.

Synthesis of OA-coated Gd/CuS nanodisks. Gadolinium-doped Gd/CuS nanodisks were synthesized according to a previous reported method for the synthesis of CuS nanodisks with modification.¹ Briefly, OA (4 mL), CuCl₂ (268.9 mg, 2 mmol) and GdCl₃·6H₂O (0.1 ~ 0.3 mmol) were put into a three-necked flask and degassed by purging nitrogen. The mixture was heat to 180 °C, to which a hot yellow solution of sulfur (2.15 ~ 2.45 mmol) and OA (8 mL) at 80 °C was swiftly injected. The solution turned to dark brown immediately after addition of sulfur. The temperature then decreased to 150 °C, and the mixture was kept stirring at 150 °C for another 30 min. Then, cold cyclohexane (20 mL) was quickly added into the solution. After cooling to room temperature, the resultant Gd/CuS nanodisks were centrifuged, washed with ethanol (10 mL) and cyclohexane (10 mL) to remove the unreacted ions and OA. The Gd/CuS nanodisks were then dispersed in cyclohexane to prepare stock solution for the synthesis of T-MAN. The molar ratio of Gd : Cu in the Gd/CuS nanodisks was determined by ICP-MS.

Synthesis of T-MAN and T-MAN-ctrl. PEGylated Gd/CuS@DSPE micelles were prepared using a well-established nanoprecipitation method. Typically, DSPE-PEG-OMe (14.4 mg) and DSPE-PEG-NH₂ (1.6 mg) were dissolved in a solution containing chloroform (9 mL) and ethanol (1 mL) in a 50 mL round-bottom flask, to which the prepared OA-coated Gd/CuS nanodisks solution (~2 mg Cu²⁺ in cyclohexane) was added. The resulting mixture was stirring at r.t. for 30 min. The solvent was then removed under vacuum to afford a dark-green film attached on the inner wall of the flask. DI water (10 mL) was then added to the flask, and the solution was kept ultrasonication at r.t. for 10 min. The resulting solution was passed through a filter (0.22 μm). Then, the PEGylated Gd/CuS@DSPE-PEG-NH₂ micelles were obtained after removal of the excess DSPE-PEG-OMe and DSPE-PEG-NH₂ via ultrafiltration (Amicon centrifugal filters, 10 kDa cutoff, 4000 rpm, 10 min). For subsequent surface modification, PEGylated Gd/CuS@DSPE-PEG-NH₂ micelles (0.5 mg Cu²⁺) were dispersed in PBS buffer (1×, pH 7.4, 1 mL), and Mal-PEG₄-NHS (10 mg/mL in 22 μL DMSO) was then added. The aqueous solution was then kept stirring at r.t. for 4 h to convert free NH₂ groups into Mal. After

removing unreacted Mal-PEG₄-NHS by ultrafiltration (Amicon centrifugal filters, 10 kDa cutoff, 4000 rpm, 10 min), the Gd/CuS@DSPE-PEG-MAL micelles were obtained, which was then dispersed in PBS buffer (1×, pH 7.4, 0.5 mL) for next conjugation. To covalently conjugate MMP-2 cleavable peptide substrate on the surface of Gd/CuS@DSPE-PEG-MAL micelles, (QSY21)-GGPLGVRGK(Cy5.5)-SS (0.12 mM, 500 μL PBS buffer, 1×, pH 7.4) was first reduced with tris(2-carboxyethyl)phosphine hydrochloride (TCEP, 1 mM) and NaHCO₃ (4 mM) at r.t. for 30 min to produce (QSY21)-GGPLGVRGK(Cy5.5)-SH. Then, the reaction solution was mixed with the solution of Gd/CuS@DSPE-PEG-MAL micelles (1×, pH 7.4, 0.5 mL), and the mixture was stirring under dark for 4 h. The unreacted (QSY21)-GGPLGVRGK(Cy5.5)-SH was then removed under ultrafiltration (Amicon centrifugal filters, 10 kDa cutoff, 4000 rpm), and (QSY21)-GGPLGVRGK(Cy5.5)-SH conjugated micells (denoted as T-MAN-ctrl) were obtained, which was followed by coupling with cRGD-SH (0.15 μmol) at r.t for another 4 h. The reaction solution was then centrifuged and washed with DI water for three times via ultrafiltration (Amicon centrifugal filters, 10 kDa cutoff, 4000 rpm, 15 min). The purified T-MAN nanoparticles were re-suspended in DI water and stored at 4 °C for further applications. The concentration of Cu²⁺ in T-MAN solution was determined by ICP-MS analysis. The amount of MMP-2 substrate (QSY21)-GGPLGVRGK(Cy5.5)-SH and cRGD-SH in T-MAN solution was determined by UV-vis and HPLC assay, respectively.

General procedure for the detection of MMP-2 with T-MAN. T-MAN (0.5 μM based on MMP-2 substrate) was dissolved in enzyme reaction buffer (TCNB buffer, 150 mM NaCl, 10 mM CaCl₂, 100 mM Tris·HCl, 0.05% Brij 35, pH = 7.4), and then incubated with recombinant MMP-2 (10 nM) at 37 °C for varying time. At each time point, the fluorescence spectra were recorded from 680 to 800 nm with the excitation of 670 nm by fluorescence scanning.

Enzyme kinetic studies of T-MAN towards MMP-2. For enzyme kinetic evaluation, we incubated different concentrations of T-MAN with a constant concentration of MMP-2 enzyme. Briefly, a series of different concentrations of T-MAN (0.031, 0.062, 0.125, 0.25, 0.5, 0.75, 1,

2, 3, and 4 μM based on MMP-2 substrate) were prepared in 100 μL MMP-2 assay buffer and placed in a 96-well black plate. The reactions were initiated upon addition of 100 μL MMP-2 (4 nM). The resulting fluorescence intensities in each well in the first five minutes were recorded on a SparkTM 10M Multimode Microplate Reader ($\lambda_{\text{ex/em}} = 660/710$ nm). The amount of T-MAN-cle at each time point was determined by a standard curve under the same conditions. Kinetic values, including K_m , V_{max} , were determined according to Michaelis-Menten equation, which was described as: $v = v_{\text{max}}[S]/(K_m+[S])$. Then, the values of k_{cat} and k_{cat}/K_m were further calculated from these two parameters.

Determination of sensitivity and specific towards MMP-2. To evaluate the sensitivity of T-MAN towards MMP-2, T-MAN (0.5 μM based on MMP-2 substrate) was incubated with varying concentrations of MMP-2 (0, 0.02, 0.05, 0.1, 0.2, 0.3, 0.4, 0.5, 0.6, 0.8, 1.0, 2.0, 3.0, 5.0, 8.0, 10, 12 and 15 nM) in enzyme reaction buffer at 37 °C for 2 h. The fluorescence spectra were then recorded from 680 to 800 nm with an excitation at 670 nm. The detection limit was calculated from $3\sigma/k$, where σ represents the standard deviation of 11 blank measurements and k represents the slope of fluorescence intensity at 690 nm towards MMP-2 concentration.

To investigate the specificity of T-MAN towards MMP-2, T-MAN (0.5 μM based on MMP-2 substrate) in TCNB assay buffer was incubated with 10 nM MMP-2, 10 nM Cathepsin B, 10 nM GGT, or 10 nM MMP-2 pretreated with SB-3CT (2 μM , 20 μM). The time-dependent fluorescence intensity at 710 nm was recorded on a microplate reader with an excitation at 660 nm. The intensity in each well was recorded every five minutes, and last for 140 min.

Measurement of longitudinal r_1 relaxivity. T-MAN or Dotarem in DI water were diluted to prepare five solutions at varying concentration of Gd^{3+} (0.03, 0.06, 0.16, 0.26, and 0.33 mM). The T_1 value in each solution was acquired on a 1 T MR scanner (NM-G1, NIUMAG) by a series of inversion-prepared fast spin-echo scans. Relaxation rates (R_1) were determined as $1/T_1$, and the exact concentrations of Gd^{3+} were determined by ICP-MS. Longitudinal relaxivities (r_1 , unit of $\text{mM}^{-1} \text{s}^{-1}$) were calculated as the slope of R_1 versus the concentration of Gd^{3+} . The T_1 -

weighted spin-echo images (TR/TE = 276.1/5.0 ms) of corresponding concentration of T-MAN and Dotarem were acquired at a 1.0 T small animal MR scanner (Bruker I-CON).

Evaluation of photothermal effect in vitro. 200 μ L PBS solutions containing different concentrations (0, 12.5, 25, 50 and 100 μ g/mL Cu^{2+}) of T-MAN in eppendorf tubes were irradiated with an 808 nm NIR laser (FC-808-10W-MM, Xilong Company, China) at varying power density (0, 0.2, 0.5, 0.8 and 1.0 W/cm^2) for 10 min. Thermal images were recorded real-time by an IR thermal camera (Fortic 225-1, Fotric), and the corresponding temperature was quantified from the IR images. To measure the photothermal conversion efficiency, 200 μ L PBS solutions containing 50 μ g/mL T-MAN in eppendorf tube was irradiated with an 808 nm NIR laser at a power density of 0.8 W/cm^2 for 7 min followed by natural cooling to room temperature with laser off.

Cell culture. Human gastric MKN45 cancer cells and human normal gastric GES-1 cells were cultured in Roswell Park Memorial Institute 1640 medium (RPMI-1640). The medium was supplemented with 10% (v/v) fetal bovine serum (FBS), 100 units per mL penicillin, and 100 units per mL streptomycin. All cells were cultured at 37 °C in a humidified atmosphere (5% CO_2).

Western blotting analysis of MMP-2 and $\alpha_v\beta_3$ integrin expression. MKN45 cells and GES-1 cells were first scraped off the plate in the presence of lysis buffer. The cells were then incubated on ice for 30 min, and the lysate was obtained by centrifugation at 13,000 \times g at 4 °C for 15 min. Aliquots of proteins were separated by SDS-PAGE (10%) and subsequently transferred to nitrocellulose membranes by electroblotting. The membrane was blocked in 5% skim milk powder in 0.1% Tris buffered saline/Tween 20 (TBST, 20 mM Tris-HCl, pH 7.4, 137 mM NaCl, and 0.1% Tween) at room temperature for 2 h, and then incubated with antibody raised against MMP-2 or $\alpha_v\beta_3$ integrin overnight at 4 °C. After three washes with TBST, the membrane was incubated with a secondary antibody horseradish peroxidase (HRP)-conjugated Goat Anti-Rabbit IgG for 2 h at room temperature. The film were developed with the ECL System. The

proteins were visualized using G:BOX chemiXR5. The resulting band intensities were quantified using an Gel-Pro32.

FL imaging of MMP-2 activity in MKN45 tumor cells and GES-1 cells. MKN45 and GES-1 cells ($\sim 5 \times 10^4$) were seeded onto a glass-bottom dish (*In Vitro* Scientific, D35-20-1-N) and allowed to grow for 12 h. After removal of medium, T-MAN (1.5 μ M based on MMP-2 substrate) was added into MKN45 and GES-1 cells in 1640 medium (0.5 mL) and incubated at 37 °C for 4 h. Moreover, T-MAN-ctrl in 1640 medium (0.5 mL) was added into MKN45 cells and incubated at 37 °C for 4 h. To inhibit MMP-2 activity, MKN45 cells were pretreated with SB-3CT (20 μ M) for 1 h. To block $\alpha_v\beta_3$ integrin, cells were pretreated with cRGD (10 μ M) for 30 min. Then T-MAN was added and incubated at 37 °C for another 4 h. After replacing the medium, fluorescence images were captured on an Olympus IX73 fluorescent inverted microscope. The fluorescence images was acquired with excitation at 650 ± 22.5 nm, and emission from 670 - 750 nm.

Colocalization studies. To examine the intracellular location of T-MAN, MKN45 cells were incubated with T-MAN (1.5 μ M based on MMP-2 substrate) for 4 h, and then costained with 0.1 μ g/mL Hoechst 33342 and 200 nM Lyso-tracker (Lyso-Tracker™ Green) for another 20 min. The medium was then removed, washed with cold PBS for three times, and the fluorescence images were acquired using the IX73 optical microscope (Olympus, Japan) equipped with DAPI, FITC and Cy5.5 filters.

In vitro cytotoxicity induced by PTT. The *in vitro* cytotoxicity was measured by methyl thiazolyltetrazolium (MTT) assay. MKN45 and GES-1 cells were seeded in 96-well cell culture plates at a density of 1×10^4 cells/wells, and allowed to grow at 37 °C for 12 h. MKN45 and GES-1 cells were then incubated with T-MAN or T-MAN-ctrl at different concentrations (0, 1, 10, 25, 50, 100, 150, 200 μ g/mL based on Cu^{2+}) for 4 h. Then, the medium was removed, and washed with cold PBS buffer for three times. Fresh RPMI-1640 medium (100 μ L) was added to wells, and MKN45 and GES-1 cells in each well were irradiated under an 808 nm laser (0.8

W/cm²) for 5 min. After irradiation, the MKN45 or GES-1 cells were kept growing for another 12 h. Cells incubated with T-MAN or T-MAN-ctrl for 12 h without laser irradiation were used to determine the dark toxicity. 3-(4,5-Dimethylthiazol-2-yl)-2,5-diphenyltetrazolium bromide (MTT) in PBS buffer (50 μ L, 1 mg/mL) was then added into each well, and the cells were incubated at 37 °C for 4 h. Then, the culture medium was removed carefully, and DMSO (100 μ L) was added into each well. The absorbance (OD) at 490 nm in each well was acquired on a microplate reader (Tcan). Each experiment was repeated for three times.

Fluorescence imaging with Calcein AM/PI staining. MKN45 cells ($\sim 5 \times 10^4$) were seeded onto a glass-bottom dish (*In Vitro* Scientific, D35-20-1-N) and allowed to grow for 24 h. For Calcein AM/PI staining, MKN45 cells were incubated with T-MAN or T-MAN-ctrl (200 μ g/mL) for 4 h. Then, the medium was removed, and washed with cold PBS buffer for three times. Fresh RPMI-1640 medium (100 μ L) was added to dishes, and MKN45 cells in each dish were treated with or without laser irradiation for 5 min (808 nm, 0.8 W/cm²). After irradiation, the MKN45 cells were kept growing for another 4 h. Then, the culture medium was removed carefully, and 1 μ M Calcein AM and 4 μ M PI were added into each dish for 30 min. The medium was then removed, washed with cold PBS for three times, and fluorescence images were acquired with an Olympus inverted fluorescence microscope. Emission from propidium iodidie was collected at red channel from 590 nm wavelength with the excitation at 540 - 580 nm, emission from Calcein AM was collected at green channel from 510 - 550 nm with excitation at 470 - 495 nm.

Animals and tumor models. BALB/c female mice at 5-6 weeks old were purchased from the Model Animal Research Center (MARC) of Nanjing University (Nanjing, China). Animal care and euthanasia were carried out with the approval of the Institutional Animal Care and Use Committee (IACUC) of Nanjing University.

To establish subcutaneous (s.c.) tumors, MKN45 cells (2.0×10^6 cells) suspended in 50 μ L of 50 v/v% mixture of matrigel in supplemented RPMI-1640 (10 % fetal bovine serum, 100 U/mL

penicillin, and 100 µg/mL streptomycin) were injected subcutaneously into the selected positions of nude mice. The length (L) and width (W) of each tumor were measured with a caliper, and the tumor volume was calculated with the formula of $V = (L \times W^2)/2$. Tumors with a single aspect of ~5-7 mm were formed after 10-15 days before used for fluorescence/MR imaging and PTT.

The orthotopic MKN45 gastric tumor model was created following an established method.^{2,3} In our experiment, MKN45 cell lines were tagged with firefly luciferase to offer bioluminescence for the monitoring of tumour growth. To establish orthotopic gastric tumor-bearing mouse models, we did the following steps. First, $\sim 10^6$ MKN45/Luc human gastric tumor cells were collected and dispersed in phosphate-buffered saline (PBS) (20 µl) mixed with Matrigel Matrix High Concentration in 1:1 ratio (Corning, NY, USA). The mouse was put in a supine position, a midline vertical incision was made in the upper abdomen and stomach was exposed to the outside of the peritoneal cavity. Then cell/matrigel suspension were injected slowly into the subserosal area of the stomach under a dissecting microscope. The injection site was pressed with a cotton swab for several minutes to prevent cell suspension effusing to unwanted regions. The stomach was then repositioned back to the peritoneal cavity carefully, and the peritoneum and skin were then sutured. Orthotopic gastric tumors formed with obvious bioluminescence signals shown in the upper abdomen after 18 days before used for fluorescence/MR imaging and PTT.

To establish lymph node metastasis models in femal nude mice, $\sim 1 \times 10^6$ MKN45 cells suspended in 40 µL phosphate buffered saline (PBS) were injected subcutaneously into the right hind foot sole of each mice.⁴⁻⁶ Three weeks later, the right popliteal lymph node swelled up, indicating the presence of metastases.

Fluorescence imaging of MMP-2 in mice. To non-invasively image MMP-2 activity in tumors, s.c. tumor bearing mice were i.v. injected with T-MAN or T-MAN-ctrl (25 µM based on MMP-

2 substrate) in 75 μ L saline solution. To inhibit MMP-2 activity or probe uptake, SB-3CT (1 mM) or free cRGD (2 mM) in 100 μ L saline was carefully injected into tumors 1 h before i.v. injection of T-MAN. Whole body fluorescence images were acquired before injection and 4 h, 8 h, 12 h, 24 h post injection.

For intraoperative optical detection of orthotopic gastric tumor tissues, nude mice were i.v. injected with T-MAN (25 μ M based on MMP-2 substrate) in 75 μ L saline solution. Then, a 1 cm sub-xiphoid midline incision was made to exposure orthotopically implanted gastric tumors for intraoperative fluorescence. Whole body fluorescence images were acquired 12 h post injection.

For noninvasive mapping of metastatic lymph nodes *in vivo*, T-MAN (25 μ L, 25 μ M based on MMP-2 substrate) was s.c. injected into the middle site of right leg, with position between the primary tumor on the footpad and metastatic LN in the inner keen. Fluorescence images were acquired before injection, and 0.5 h, 1 h, 2 h, 4 h following s.c injection.

The whole body fluorescence images at indicated time point were acquired on an IVIS Lumina XR III imaging system, using a 660 nm excitation filter and a 710 nm emission filter. Each experiment was conducted in three mice. The fluorescence intensities were quantified by the ROIs measurement using Living Image Software (4.5.2, PerkinElmer, MA, U.S.A).

Noninvasive MR imaging of tumors in mice. For T_1 -weighted MR imaging of s.c. tumors *in vivo*, nude mice were i.v. injected with T-MAN or T-MAN-ctrl (0.05 mmol/Kg based on Gd^{3+}) in 100 μ L saline solution. To inhibit MMP-2 activity or probe uptake, SB-3CT (1 mM) or free cRGD (2 mM) in 100 μ L saline was injected into tumors 1 h before i.v. injection of T-MAN. Whole body MR images were acquired before injection and 12 h post injection.

For T_1 -weighted MR imaging of orthotopic gastric tumors, nude mice were i.v. injected with T-MAN (0.05 mmol/Kg based on Gd^{3+}) in 100 μ L saline solution. MR images were acquired before injection and 12 h post injection.

For T_1 -weighted MR imaging of metastatic lymph nodes, T-MAN (0.025 mmol/Kg based on Gd^{3+}) in 25 μ L saline solution was s.c. injected into the middle site of right leg, with position between the primary tumor on the footpad and metastatic LN in the inner knee. MR images were acquired before injection, and 0.5 h, 1 h, 2 h, 4 h following s.c injection.

All the MR imaging experiments were conducted on a 1.0 T small animal MR scanner (Bruker I-CON). The images were acquired using a T_1 -RARE imaging sequence. The detailed MR imaging parameters were as follows: repetition time ms/echo time ms, 446/15.0; image size, 256 \times 256; slice thickness 1.000 mm; slices, 10; field of view, 35 mm \times 35 mm. The acquisition time for each MR imaging was 11 min 25 s. Each experiment was conducted in three mice. Acquired MRI data were then transferred as DICOM images to an RadiAnt DICOM Viewer for quantitative image analysis. This consisted of manual segmentation of the tumor and lymph node ROI for every image at each time point to generate mean volumetric signal intensities (SI). Percentage signal enhancement (% SE) was calculated at each time point as the % difference between the tumor or lymph node SI in the precontrast data set.

Bioluminescence imaging of the orthotopic gastric tumors. *In vivo* imaging of orthotopic gastric tumor-bearing mice were carried out using bioluminescence imaging modality. Mice were intraperitoneally injected with 150 mg/kg weight of D -luciferin (R&D Systems) 10 min prior to being imaged under gaseous anesthesia with isoflurane using an an IVIS Lumina XR III system.

Fluorescence Imaging of Tissue Slices. For fluorescence imaging of tumor tissue slices, MKN45 tumor-bearing mice were sacrificed and the tumor were resected at 12 h post i.v. injection of T-MAN or T-MAN-ctrl (25 μ M based on MMP-2 substrate). For fluorescence imaging of lymph node tissue slices, mice with or without lymph node metastasis were sacrificed and the lymph nodes were resected at 2 h post s.c. injection of T-MAN into the middle site of right leg, with position between the primary tumor on the footpad and metastatic LN in

the inner keen. The isolated tumors and lymph nodes tissues were cut using a vibrating-blade microtome to obtain 10 μm -thickness slices. After staining with DAPI, the images of tumor or lymph node tissue slices were acquired with the IX73 fluorescent inverted microscope equipped with DAPI and Cy5.5 filters.

In Vivo PTT of tumor and LN Metastasis. For *in vivo* PTT of s.c. tumors, mice bearing s.c. MKN45 tumors were randomly divided into six groups (n = 5 per group): (i) PBS only, (ii) PBS and laser irradiation, (iii) T-MAN (5 mg/Kg Cu^{2+}) only, (iv) T-MAN-ctrl (5 mg/Kg Cu^{2+}) only, (v) T-MAN-ctrl and laser irradiation, (vi) T-MAN and laser irradiation. Mice were i.v. injected with 100 μL PBS, T-MAN or T-MAN-ctrl. After 12 h, the tumors were irradiated by the 808 nm laser (0.8 W/cm^2) for 10 min. An IR thermal camera (Fortic 225-1) was used to monitor the temperature changes in mice during laser irradiation. The length (L) and width (W) of each tumor were measured with a caliper, and the tumor volume was calculated with the formula of $V = (L \times W^2)/2$. The tumor volume and body weight in each mouse were measured in every two days, and monitored up to 16 days. The relative tumor volumes were calculated for each mouse as V/V_0 (V_0 was the tumor volume when the treatment was initiated). On day 16, all the mice were sacrificed, and the tumors were excised from the mice and photographed.

For PTT of orthotopic MKN45/Luc gastric tumors, mice bearing orthotopic tumors were divided into two groups (n = 5 per group): (I) No treatment (control group) and (II) T-MAN and laser irradiation. T-MAN (5 mg/Kg Cu^{2+}) in 100 μL PBS was i.v. injected into mice. After 12 h, Intraoperative PTT of orthotopic gastric tumors was conducted in living mice. Briefly, stomachs with implanted gastric tumors were exposed by a 1 cm sub-xiphoid midline incision, and the tumor locations delineated by both BL and FL imaging were carefully irradiated with the 808 nm laser (0.85 W/cm^2) for 10 min. After irradiation, the stomachs were repositioned back to the peritoneal cavity carefully, and the peritoneum and skin were then sutured. To monitor the therapeutic effect, mice following treatment were i.p. injected with D -luciferin, and

the whole body BL images were recorded every 4 days, and lasted for 16 days. On day 16, T-MAN (0.05 mmol/Kg based on Gd^{3+}) was i.v. injected into mice. After 12 h, both coronal and axonal T_1 -weighted MR images of mice were acquired to noninvasively monitor the PTT effect against orthotopic gastric tumors. Then, all mice were sacrificed, and BL images and weights of excised orthotopic gastric tumors were measured.

For PTT of LN metastasis, mice with MKN45 lymph node metastasis were randomly divided into four groups (n = 5 per group) including: (I) PBS only, (II) PBS and laser irradiation, (III) T-MAN only and (IV) T-MAN and laser irradiation. PBS (25 μ L) or T-MAN (25 μ L, 2.5 mg/Kg Cu^{2+}) was s.c. injected into the middle site of right leg, with position between the primary tumor on the footpad and metastatic LN in the inner knee. After 1 h, the metastasis LNs were irradiated with the 808 nm laser (0.5 W/cm²) for 10 min. Real-time *in vivo* temperature changes were recorded with an IR thermal camera (Fortic 225-1, Fotric, China). On day 16, all the mice were sacrificed, and the lymph nodes were excised from the mice photographed and weighted.

Biodistribution studies. Nine mice bearing s.c. MKN45 tumors were i.v. injected with T-MAN (5 mg/Kg Cu^{2+}). Every three mice were sacrificed at 4, 12 and 24 h. Tumors and major organs including heart, liver, spleen, lung, kidneys were collected and weighed. The tissues were cut into small pieces, and digested with concentrated HNO_3 under heating at 120 °C overnight. The residue in each organ was then diluted with 5 mL 2% HNO_3 solution, and the concentration of Cu^{2+} was determined by ICP-MS. The %ID/g was also calculated for comparison.

Histopathological analysis. Histopathological analysis was performed on MKN45 in s.c. tumor-bearing mice or mice with LN metastasis. One day post treatment, MKN45 s.c. tumors or metastatic LNs from mice following indicated treatments were excised, and fixed in formalin. Then, the tumor or LN tissues were cryosectioned at 10- μ m thickness and stained with H&E or TUNNEL (KeyGen Biotech. Co. Ltd., Nanjing, China) staining kit according to the manufacturer's instructions. The images were acquired on an IX73 optical microscope

(Olympus, Japan) equipped with a color camera. To examine the potential side effects, major organs including liver, spleen, kidney, heart, lung from treated mice were collected 16 days post treatment, and applied for histopathological analysis.

Statistical analysis. Student's t test was used for between two-group comparison and oneway ANOVA with Fisher's LSD for multiple-group analysis. $p < 0.05$ was considered to be statistical significance. The statistical tests were run with SPSS 16.0 (SPSS Inc., Chicago, IL).

Supplementary Figures

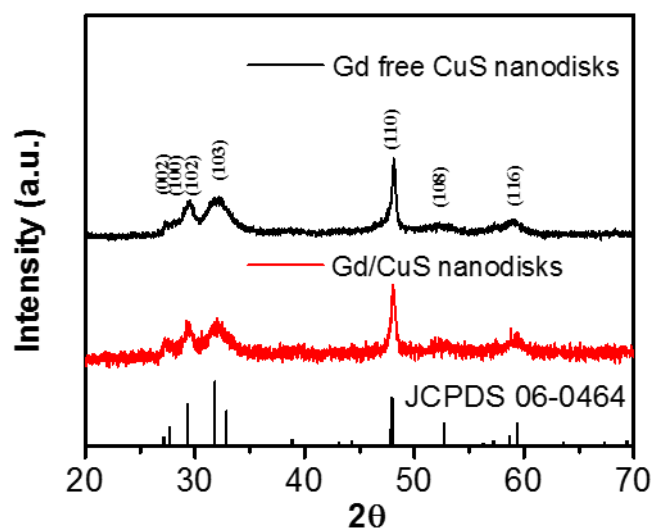


Figure S1. Powder X-ray diffraction patterns of Gd free CuS nanodisks (black) and Gd/CuS nanodisks (red), as referenced by the standard CuS covellite phase (JCPDS 06-0464).

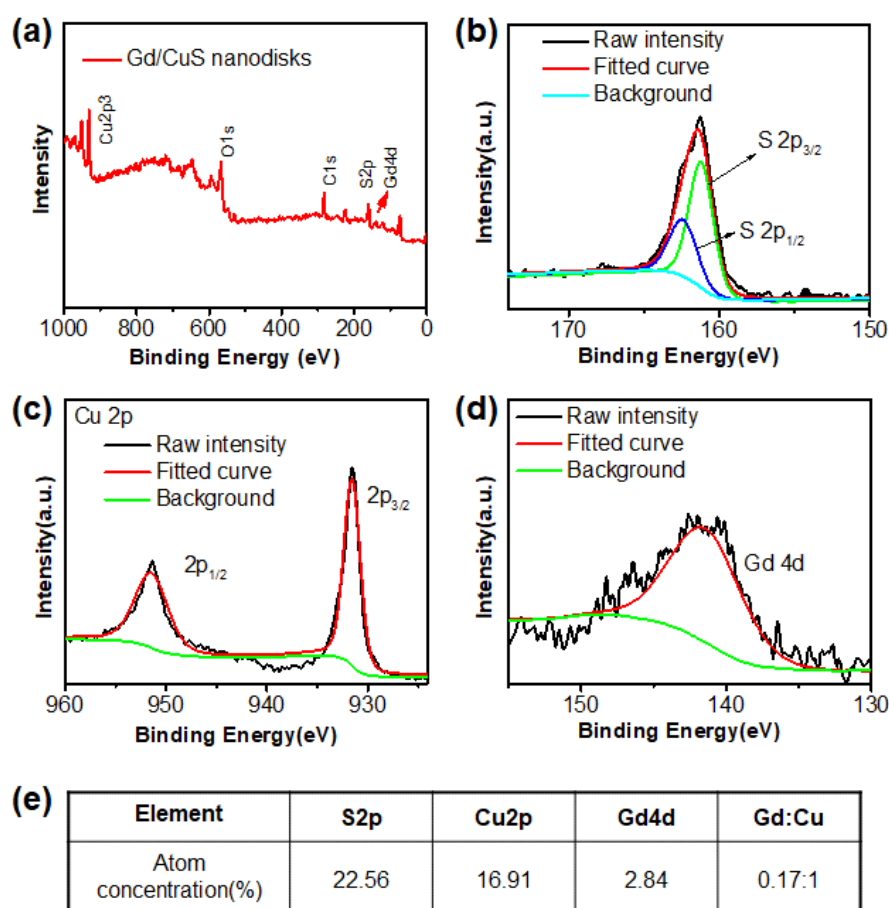


Figure S2. XPS spectra and element atom concentration of the as-prepared Gd/CuS nanodisks. (a) Survey spectra, (b) high-resolution scan of S2p, (c) high-resolution scan of Cu2p, (d) high-resolution scan of Gd4d, (e) atom concentration of S2p, Cu2p and Gd4d.

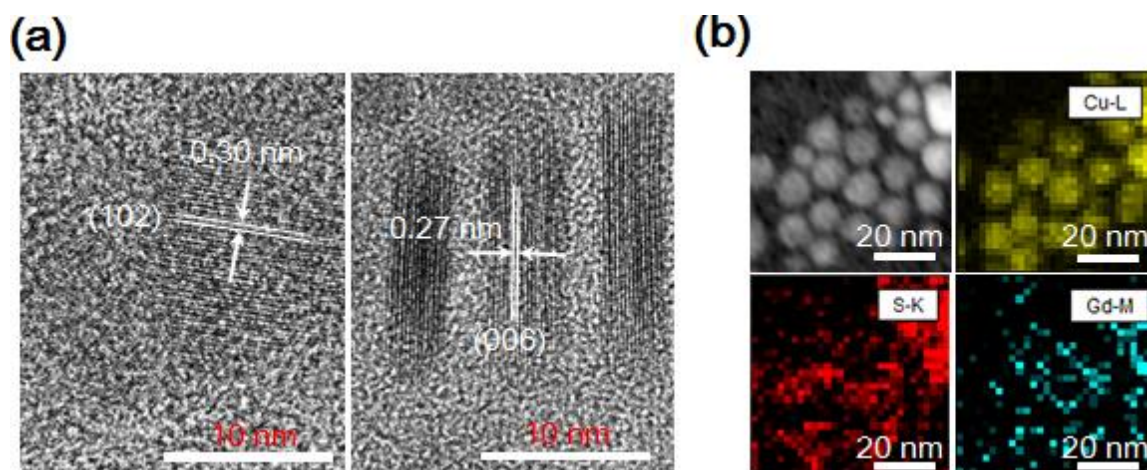


Figure S3. (a) HRTEM images of Gd/CuS nanodisks lying parallel (left) or perpendicular (right) to the substrate. (b) Elemental mapping images show the presence of Cu, S and Gd elements in the Gd/CuS nanodisks.

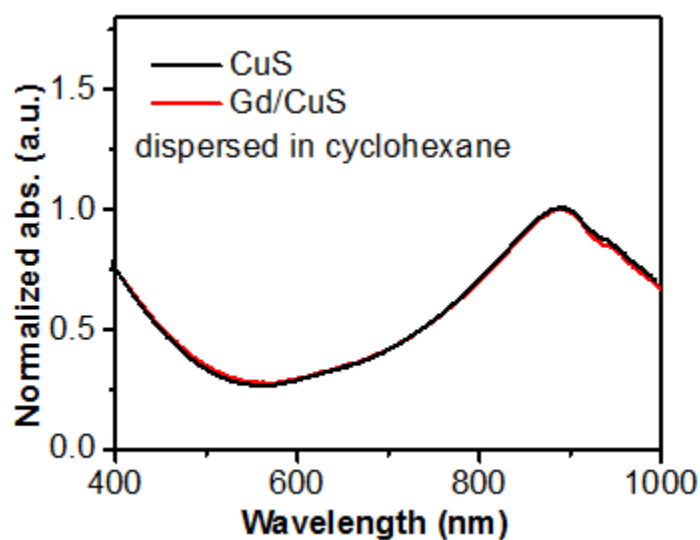


Figure S4. UV-vis-NIR absorption spectra of the Gd/CuS and CuS in cyclohexane.

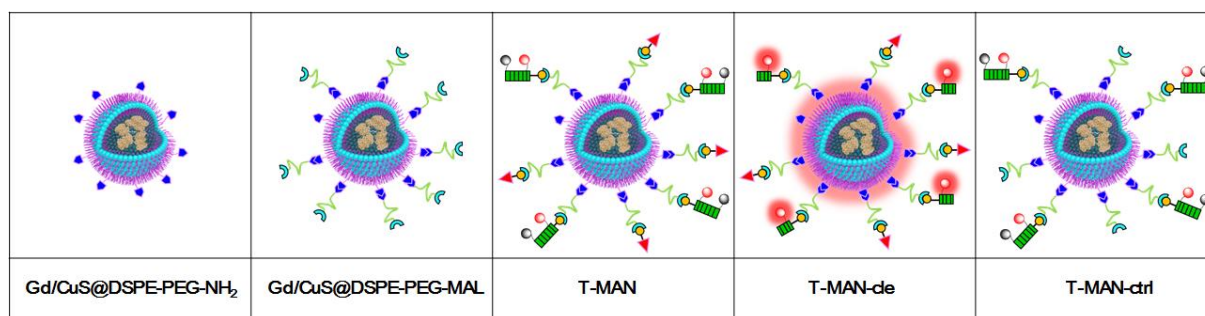


Figure S5. Cartoon illustration of Gd/CuS@DSPE-PEG-NH₂, Gd/CuS@DSPE-PEG-MAL, T-MAN, T-MAN-cle and T-MAN-ctrl.

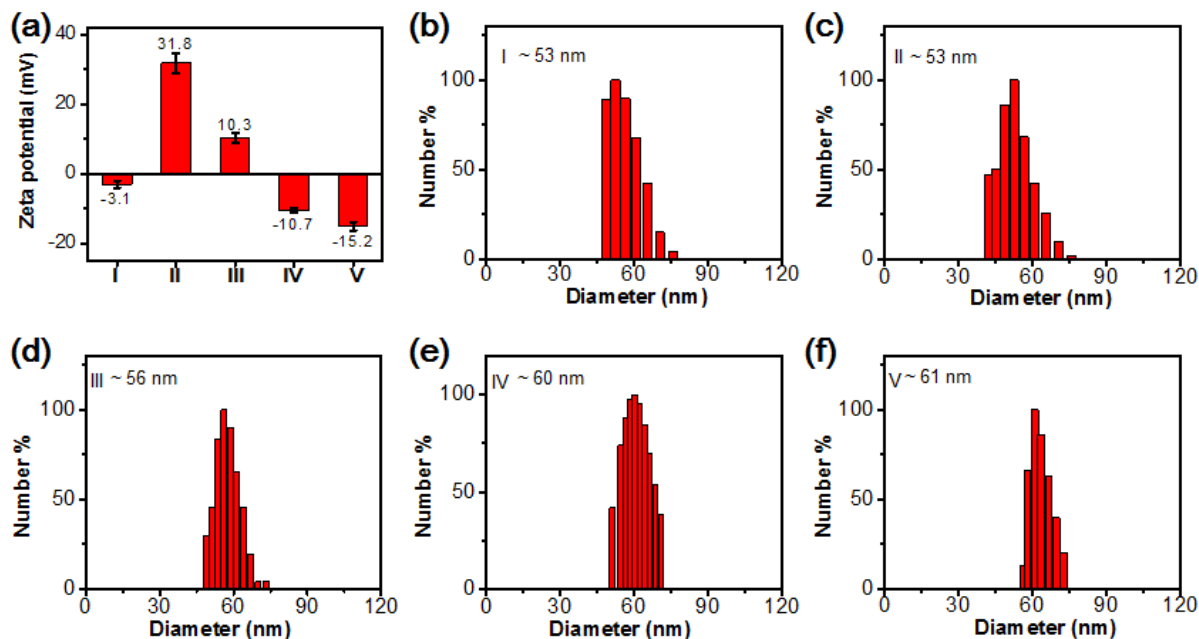


Figure S6. Nanocharacterization of as-prepared nanoparticles. (a) Zeta potentials, (b-f) DLS analysis of hybrid Gd/CuS@DSPE micellar nanoparticles with different surface modifications: I: Gd/CuS@DSPE-PEG-OMe; II: Gd/CuS@DSPE-PEG-NH₂; III: Gd/CuS@DSPE-PEG-MAL; IV: T-MAN-ctrl; V: T-MAN.

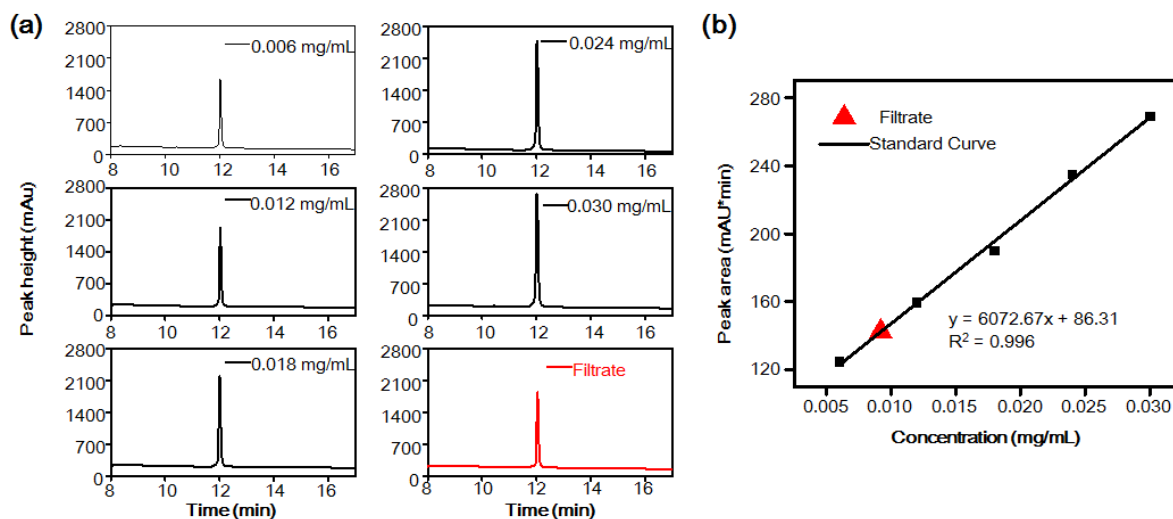


Figure S7. (a) HPLC analysis of different concentrations of cRGD and cRGD in the filtrate. (b) Linear fitting curve of the peak area with the concentration of cRGD ranging from 0.006-0.03 mg/mL. The red triangle indicates the concentration of cRGD in the filtrate.

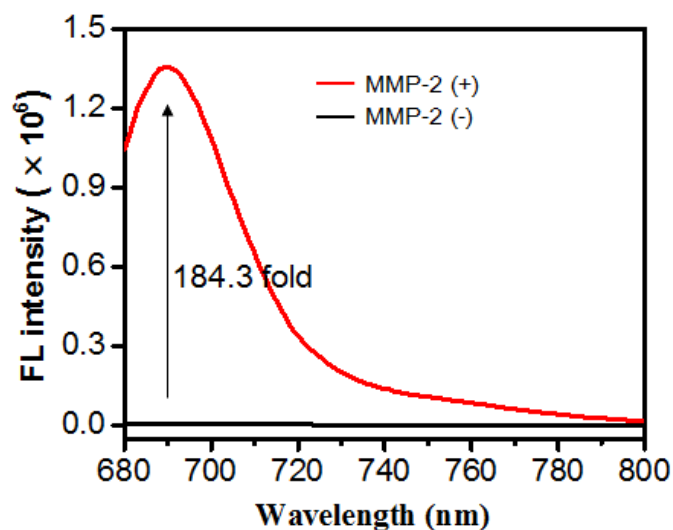


Figure S8. Fluorescence spectra of (QSY21)-GGPLGVRGK(Cy5.5)-SH following incubation with (red) or without (black) MMP-2 in enzyme reaction buffer at 37 °C for 2 h.

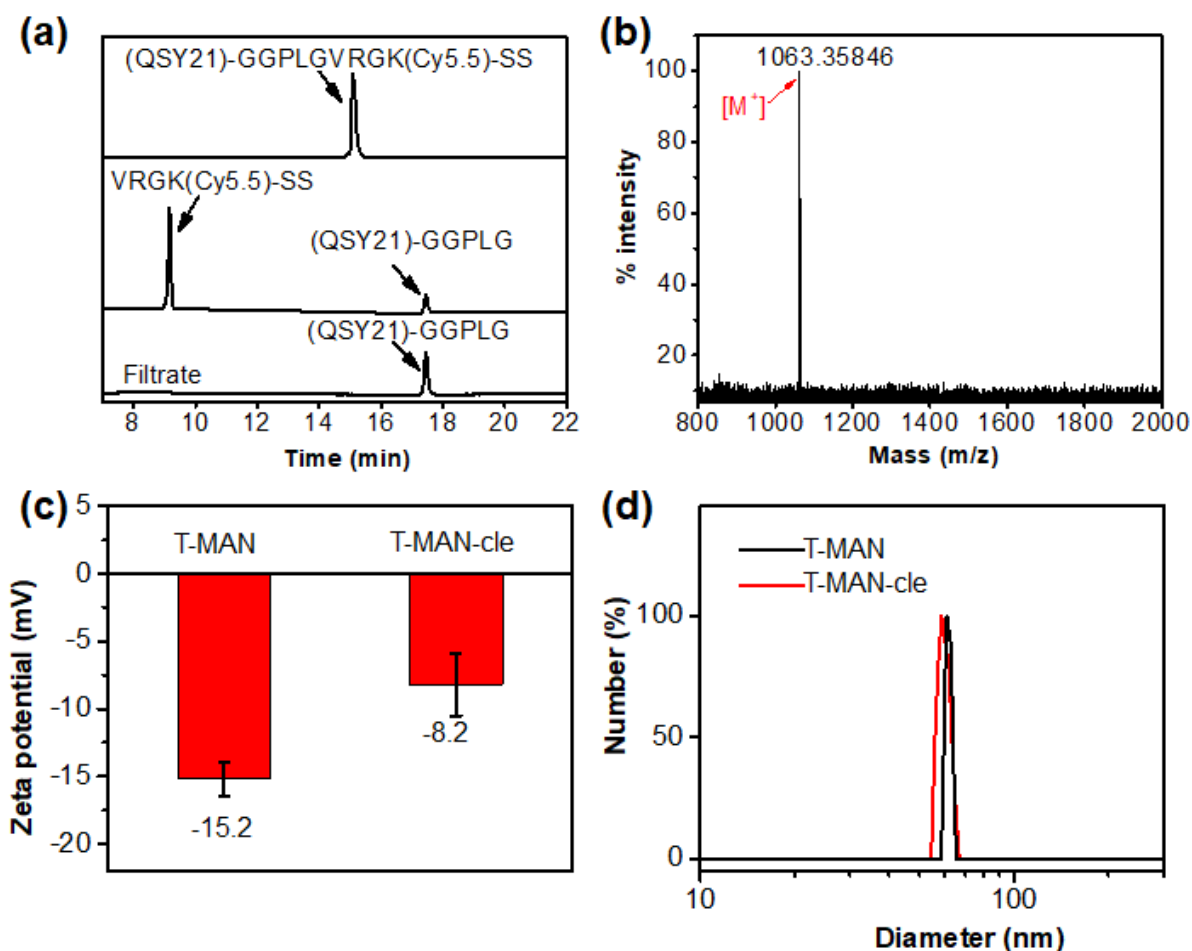


Figure S9. Analysis of the reaction between T-MAN and MMP-2. (a) HPLC spectra of free MMP-2 substrate ((QSY21)-GGPLGVRGK(Cy5.5)-SS) (HPLC retention time $T_R = 15.1$ min, black), (QSY21)-GGPLGVRGK(Cy5.5)-SS following incubation with MMP-2 (10 nM) for 2 h (blue), or the filtrate of T-MAN following incubation with MMP-2 (10 nM) for 2 h (red). The

HPLC peaks with T_R of 9.1 and 17.4 min were assigned to the cleaved product VRGK(Cy5.5)-SS and (QSY21)-GGPLG, respectively. (b) High-resolution MALDI-MS analysis of the HPLC peak ($T_R = 17.4$ min) in filtrate of T-MAN after incubation with MMP-2 (10 nM) at 37 °C for 2 h. Calcd. (QSY21)-GGPLG $C_{58}H_{63}N_8O_{10}S^+$, 1063.4382, found 1063.3585. (c) Zeta potentials and (d) DSL analysis of (T-MAN) and the cleaved nanoparticle T-MAN-cle.

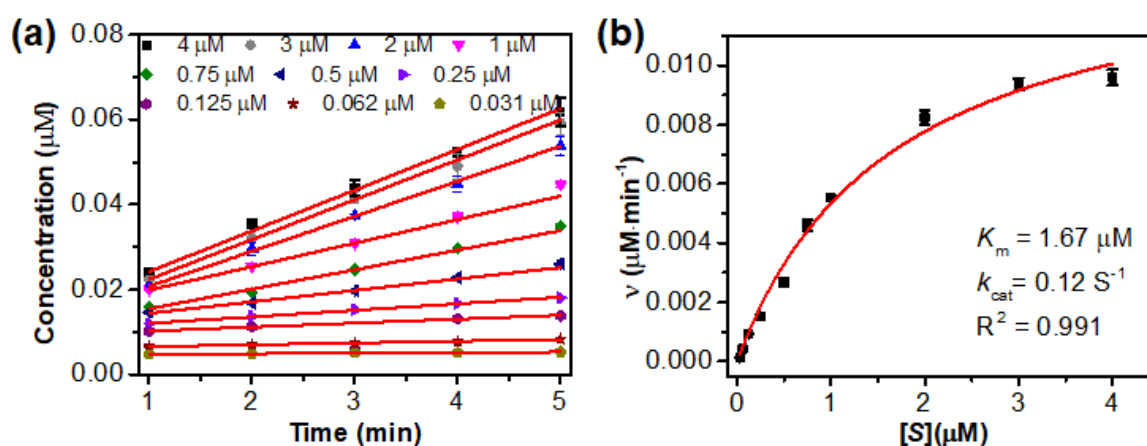


Figure S10. Evaluation for the kinetics parameters of T-MAN toward MMP-2. (a) Plots of the concentrations of T-MAN-cle versus incubation time. T-MAN-cle was generated from the incubation of varying concentrations of T-MAN with MMP-2 (10 nM) in enzyme reaction buffer at 37 °C for 5 min. (b) Michaelis-Menten plots of T-MAN with MMP-2. Error bars represent standard deviations ($n = 3$).

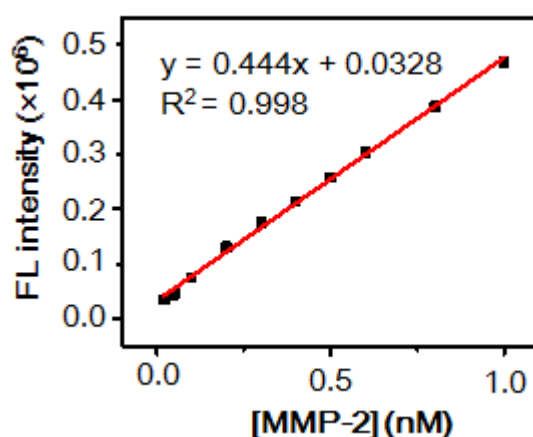


Figure S11. Linear fitting curve of FL intensity ($\lambda_{\text{em}} = 690$ nm) versus the concentration of MMP-2 from 0.02-1.0 nM. The detection limit was calculated to be ~ 0.64 pM (single to-noise, $S/N = 3$).

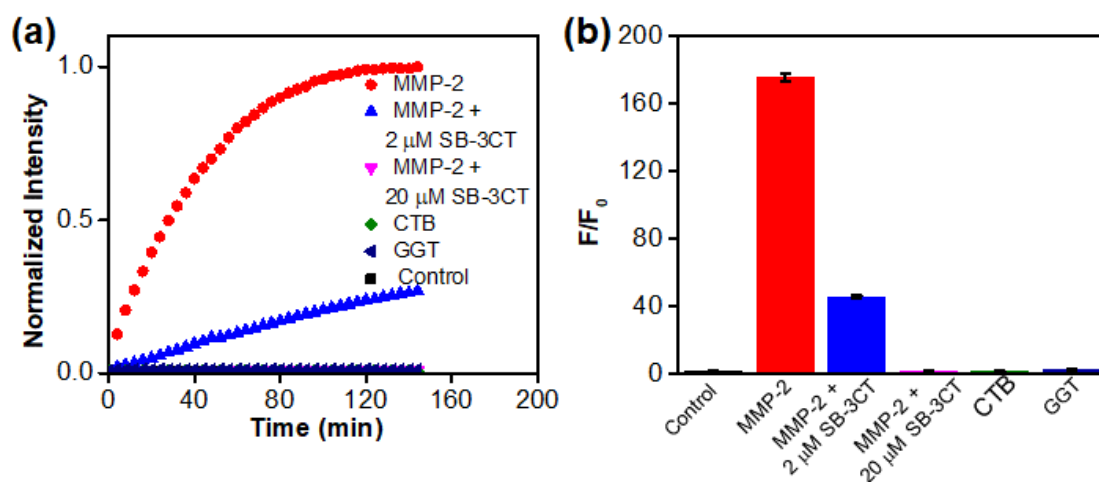


Figure S12. Investigation of the specificity of T-MAN toward MMP-2. (a) Time-dependent fluorescence intensity changes of the solution containing T-MAN (0.5 μM) alone (Control), T-MAN plus MMP-2 (10 nM), T-MAN plus MMP-2 (10 nM) and its inhibitor SB-3CT (2 μM or 20 μM), T-MAN with 10 nM GGT, or T-MAN with Cathepsin B in enzyme reaction buffer for 2 h. $\lambda_{\text{ex/em}} = 660/710$ nm. (b) The fluorescence turn-on ratio (F/F_0) of T-MAN (0.5 μM) after incubation with indicated reagents for 2 h. Error bars represent standard deviation ($n = 3$).

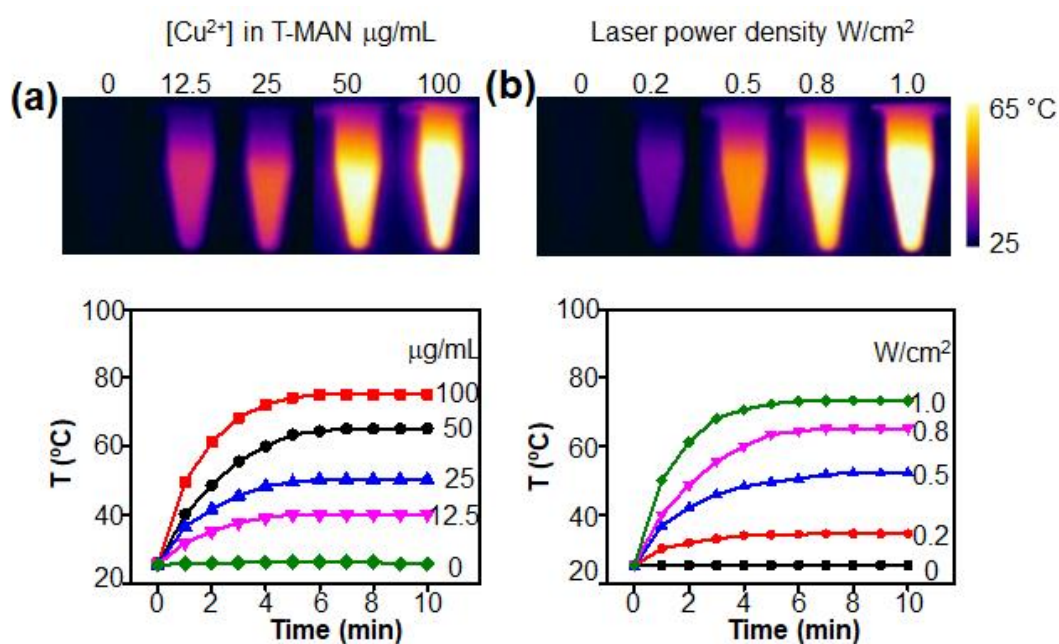


Figure S13. (a) Temperature increase of varying concentrations of T-MAN (0~100 μg/mL Cu²⁺) under 808 nm laser irradiation (0.8 W/cm²) for 0-10 min. (b) Temperature increase of T-MAN (50 μg/mL Cu²⁺) following 808 nm laser irradiation at varying power densities (0~1 W/cm²) for 0-10 min.

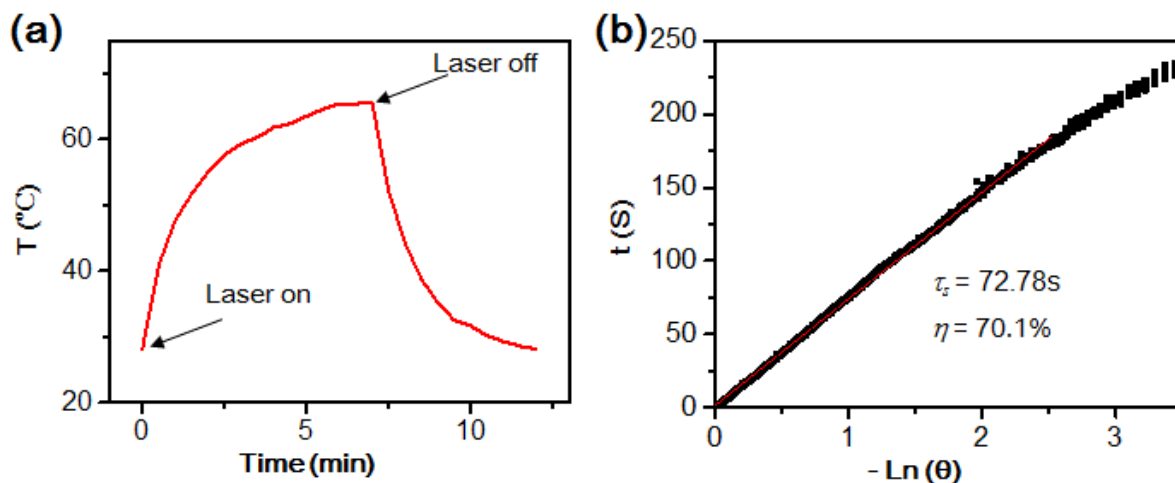


Figure S14. Measurement of photothermal conversion efficiency. (a) Photothermal effect of a T-MAN aqueous solution upon irradiation with an 808 nm laser, and the laser was turned off after irradiation for 7 min. (b) Obtained time constant for heat transfer of this system ($\tau_s = 72.78$ s) by applying linear time data versus $\ln \theta$ from the cooling stage. The photothermal conversion efficiency was calculated to be $\sim 70.1\%$, according to the method list in Note S3.

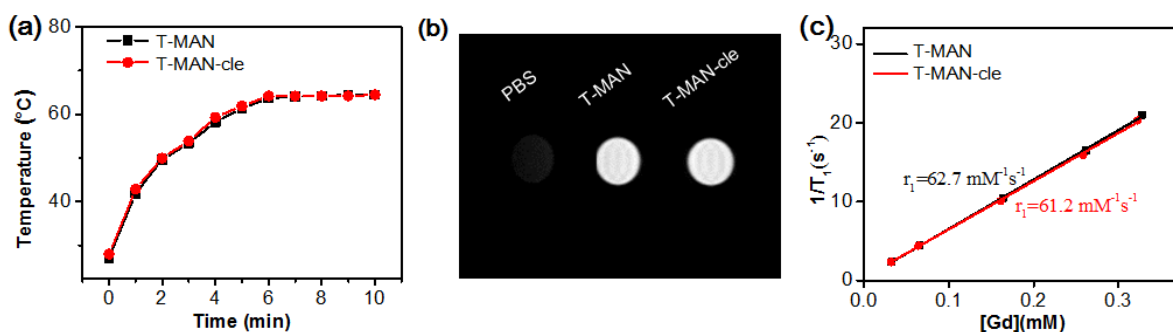


Figure S15. Comparison of the photothermal effect and MR property between T-MAN and T-MAN-cle. (a) Temperature increase of aqueous solution containing T-MAN ($50 \mu\text{g/mL Cu}^{2+}$) and T-MAN-cle ($50 \mu\text{g/mL}$ based on Cu^{2+}). (b) T_1 -weighted MR images of PBS buffer, PBS buffer containing T-MAN (0.33 mM Gd^{3+}), and PBS buffer containing T-MAN-cle (0.33 mM based on Gd^{3+}). (c) Plots of $1/T_1$ of T-MAN and T-MAN-cle versus Gd^{3+} concentration at 0.5 T ($\text{TE/TR} = 18/120 \text{ ms}$, NMI20-015 V-I, NIUMAG). T-MAN-cle was generated from incubation of T-MAN with MMP-2 for 2 h.

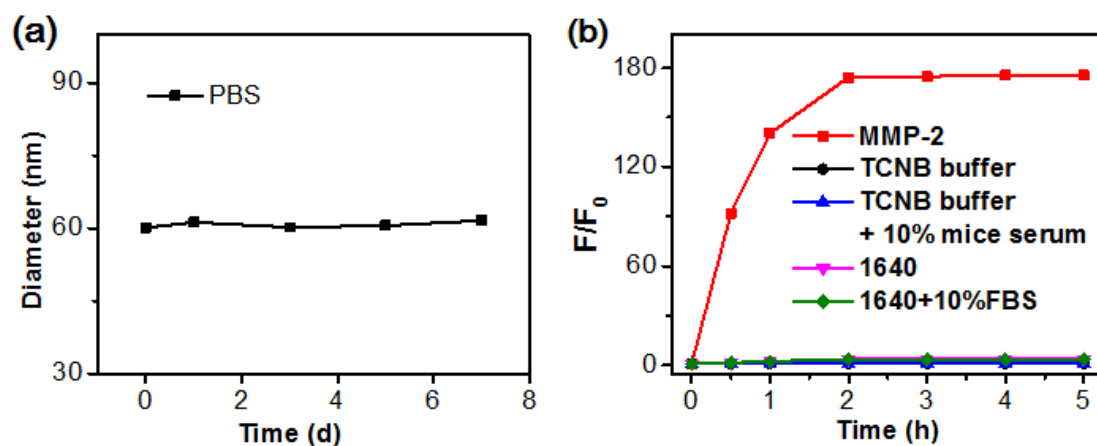


Figure S16. Investigation of the stability of T-MAN. (a) DLS analysis of T-MAN incubated in PBS buffer at r.t. for over 7 days. (b) Time-dependent fluorescence turn-on ratio (F/F_0) of T-MAN ($0.5 \mu\text{M}$) following incubation in TCNB buffer, TCNB buffer containing 10 nM MMP-2 or 10% mice serum, 1640 cell culture medium, or 1640 medium containing 10% FBS for different time. ($\lambda_{\text{ex/em}} = 660/710 \text{ nm}$).

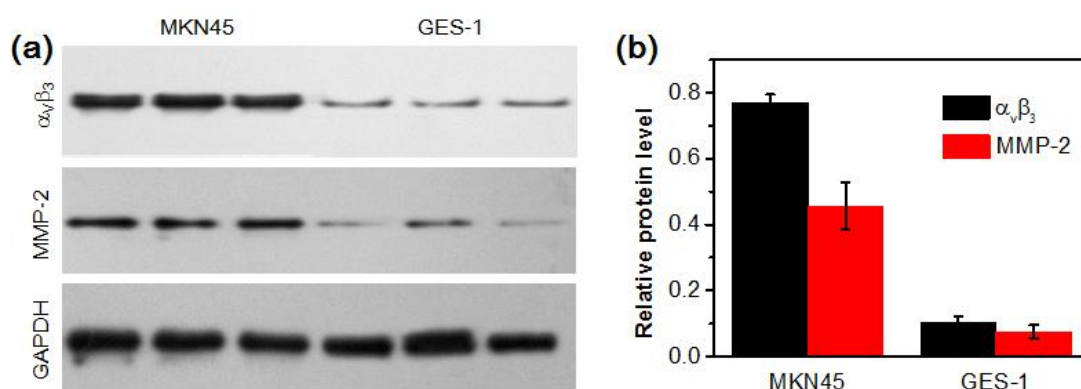


Figure S17. Investigation of $\alpha_v\beta_3$ and MMP-2 expression in MKN45 and GES-1 cells. (a) Evaluation of $\alpha_v\beta_3$ and MMP-2 protein level by Western blot analysis in MKN45 cells and normal gastric GES-1 cells. (b) Quantification of the relative $\alpha_v\beta_3$ and MMP-2 levels based on the Western blot results. The $\alpha_v\beta_3$ and MMP-2 level in each band was quantified using Gel-Pro32 and qualified against the band of GAPDH. Error bars indicated standard deviation from three experiments. These results revealed that MKN45 tumor cells have much higher expression of $\alpha_v\beta_3$ and MMP-2 compared to that of GES-1 normal stomach cells.

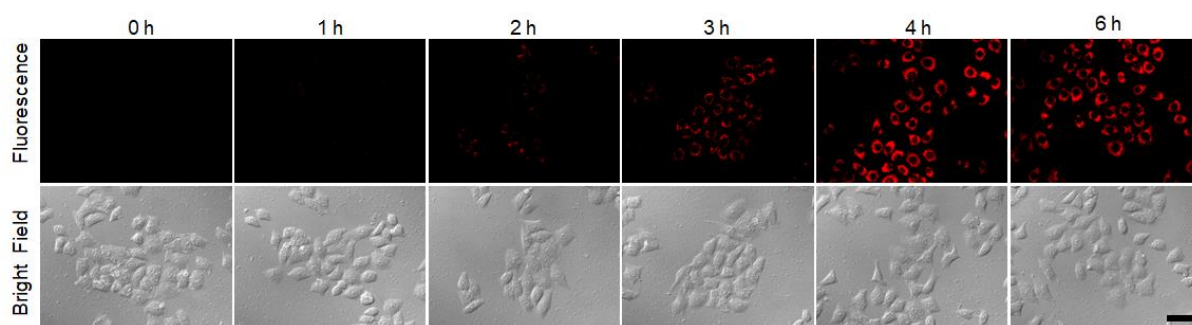


Figure S18. Fluorescence images of MKN45 cells following incubation with T-MAN ($1.5 \mu\text{M}$) for 0, 1, 2, 3, 4, and 6 h. The images were acquired on an inverted fluorescent microscope after removing the incubation medium. Scale bars: $50 \mu\text{m}$. The fluorescence images showed that the fluorescence inside MKN45 cells became maximum after incubation for 4 h.

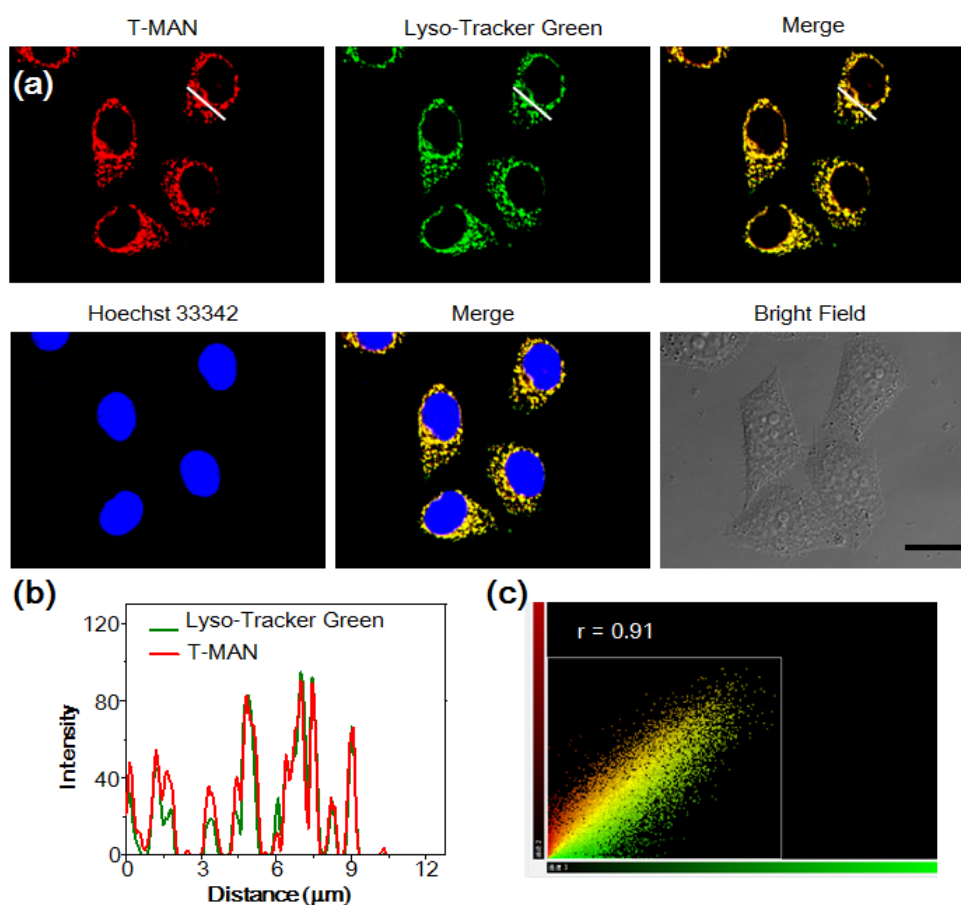


Figure S19. Colocalization studies of MKN45 cells following incubation with T-MAN and the Lyso-tracker. (a) Fluorescence images of MKN45 cells following incubation with T-MAN ($1.5 \mu\text{M}$) for 4 h and then co-stained with 200 nM Lyso-Tracker Green for 20 min. Scale bar: $20 \mu\text{m}$. (b) Average intracellular fluorescence intensity of MKN45 cells as shown in the images of (a). (c) The scatter plot of Red (T-MAN) and Green (Lyso-Tracker) channels using cellSens Dimension software, with the Pearson's correlation coefficient (r) found to be 0.91.

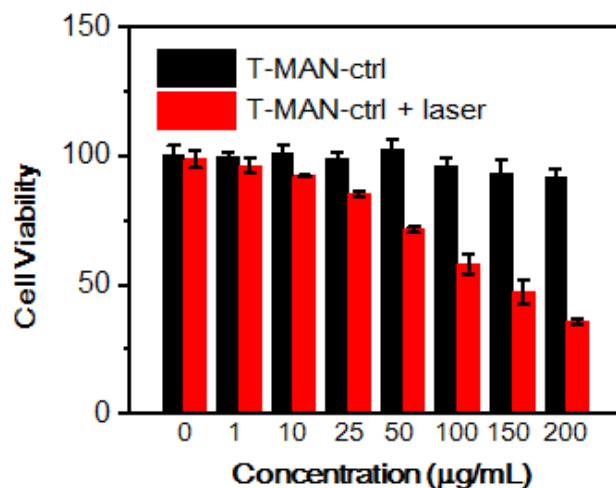


Figure S20. Viabilities of MKN45 cells incubated with different concentrations of T-MAN-ctrl (Cu^{2+} : 0, 1, 10, 25, 50, 100, 150, 200 $\mu\text{g/mL}$) in the absence or presence of laser irradiation (808 nm, 0.8 W/cm^2 , 5 min).

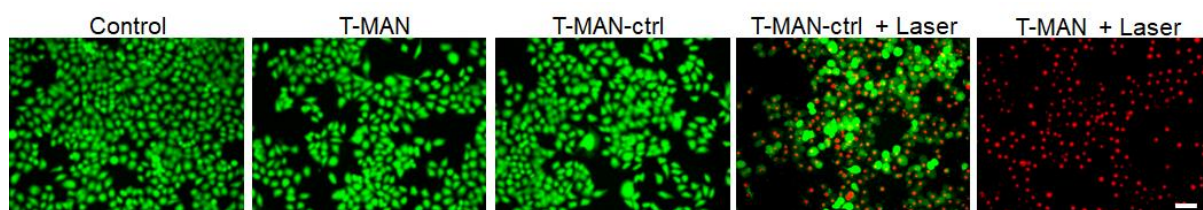


Figure S21. Fluorescence images of Calcein AM (green color, live) and PI (red color, dead) co-stained MKN45 cells following treatment with T-MAN or T-MAN-ctrl (200 $\mu\text{g/mL}$ Cu^{2+}) in the absence or presence of laser irradiation (808 nm, 0.8 W/cm^2) for 5 min. Scale bar: 20 μm .

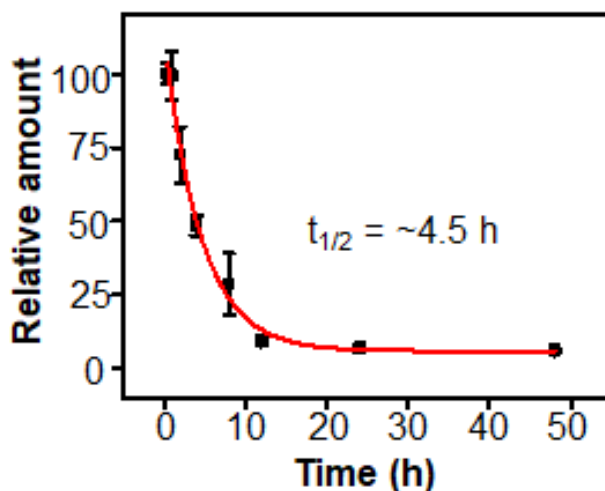


Figure S22. Blood circulation curve of T-MAN in mice ($n = 4$).

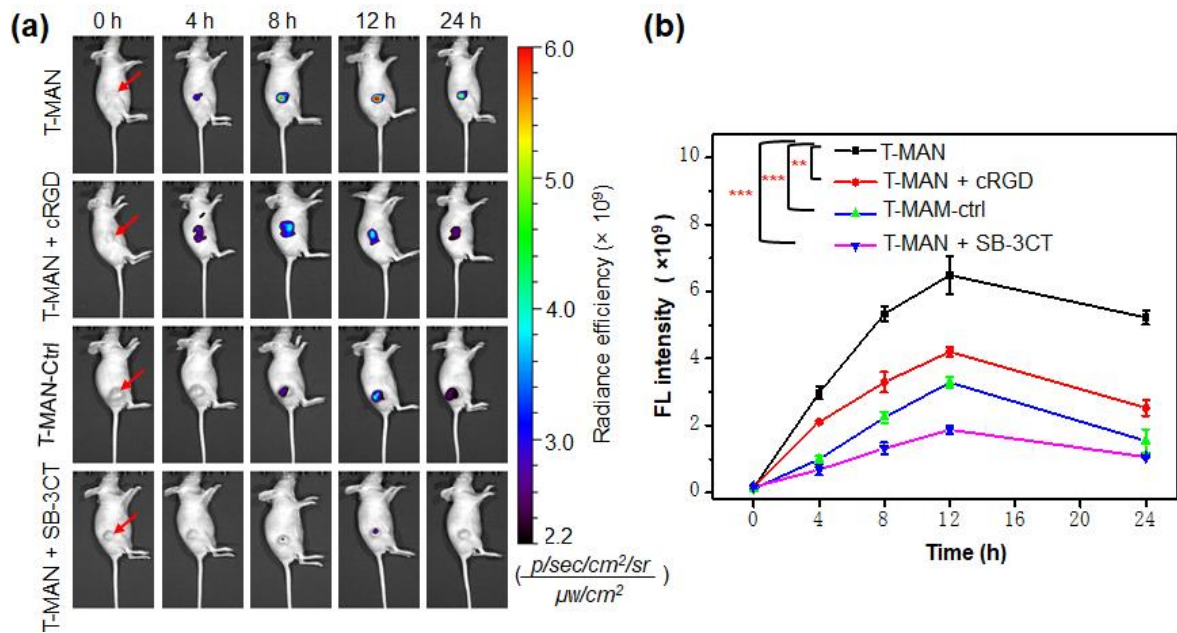


Figure S23. (a) Fluorescence images ($\lambda_{ex/em} = 660/710$ nm) and (b) average FL intensities (0 h, 4 h, 8 h, 12 h and 24 h) of s.c. MKN45 tumors in living mice receiving: i.v. injection of T-MAN (25 μ M MMP-2 substrate, 75 μ L), i.t. injection of free cRGD (2 mM, 100 μ L) followed by i.v. injection of T-MAN 1 h later, i.v. injection of T-MAN-ctrl (25 μ M based on MMP-2 substrate, 75 μ L), and i.t. injection of MMP-2 inhibitor SB-3CT (1 mM, 100 μ L) followed by i.v. injection of T-MAN 1 h later. Red arrows indicate the location of tumors. ** $p < 0.01$; *** $p < 0.001$.

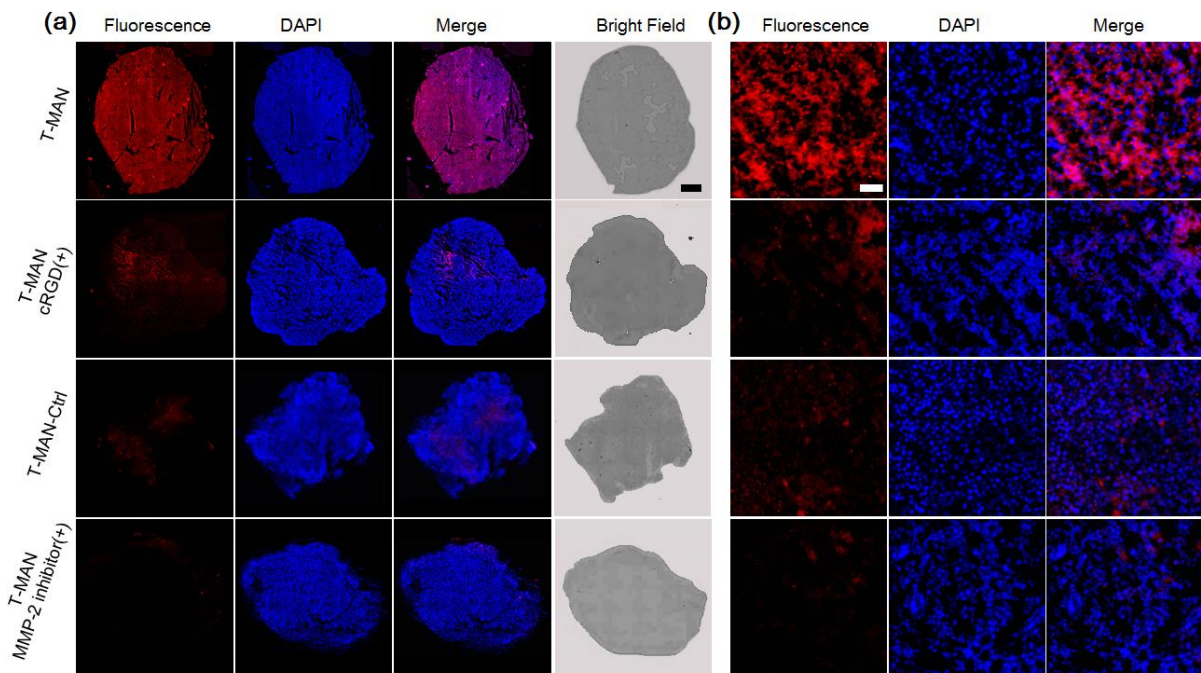


Figure S24. *Ex vivo* fluorescence images of whole frozen tumor tissue slices (a) and corresponding enlarged images (b) resected from MKN45 tumor bearing mice at 12 h post i.v.

injection of T-MAN (25 μ M MMP-2 substrate, 75 μ L), T-MAN plus i.t. injection of free cRGD (2 mM, 100 μ L), T-MAN-ctrl or T-MAN plus i.t. injection of SB-3CT (1 mM, 100 μ L). Black scale bar: 1 mm; white scale bar: 50 μ m.

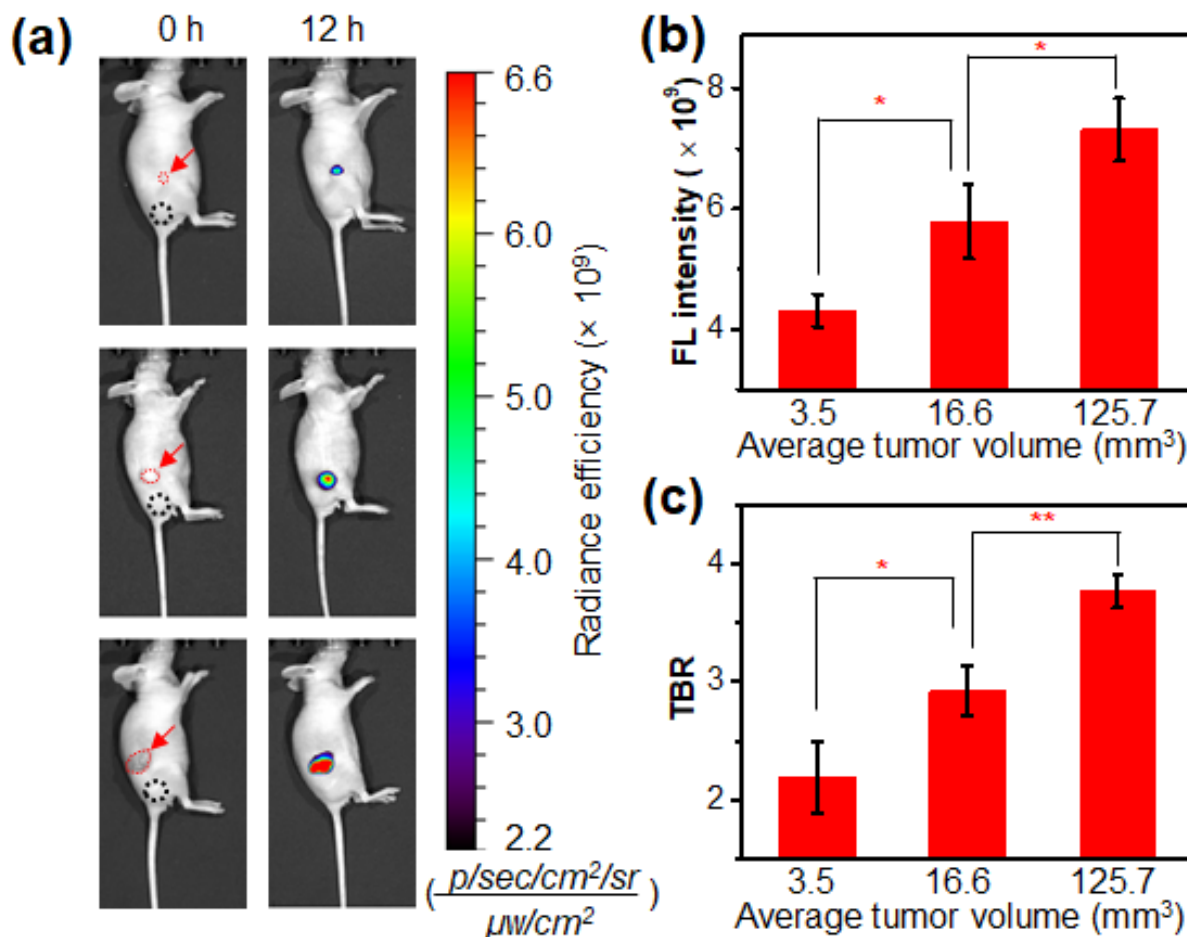


Figure S25. (a) Fluorescence imaging ($E_x/E_m = 660/710$ nm) of s.c. MKN45 tumors with different sizes *in vivo*. Mice bearing different size of s.c. MKN45 tumors were i.v. injected with T-MAN (25 μ M MMP-2 substrate, 75 μ L). The fluorescence images were acquired before (0 h) and 12 h post injection. (b) Average tumor fluorescence intensities and (c) tumor-to-background (TBR) in different size of MKN45 tumors-bearing mice at 12 h after injection of T-MAN. Values were mean \pm SD ($n = 3$). * $p < 0.05$, ** $p < 0.01$. Red arrows and circles indicate the location of tumors. Black circles indicate the locations selected for background

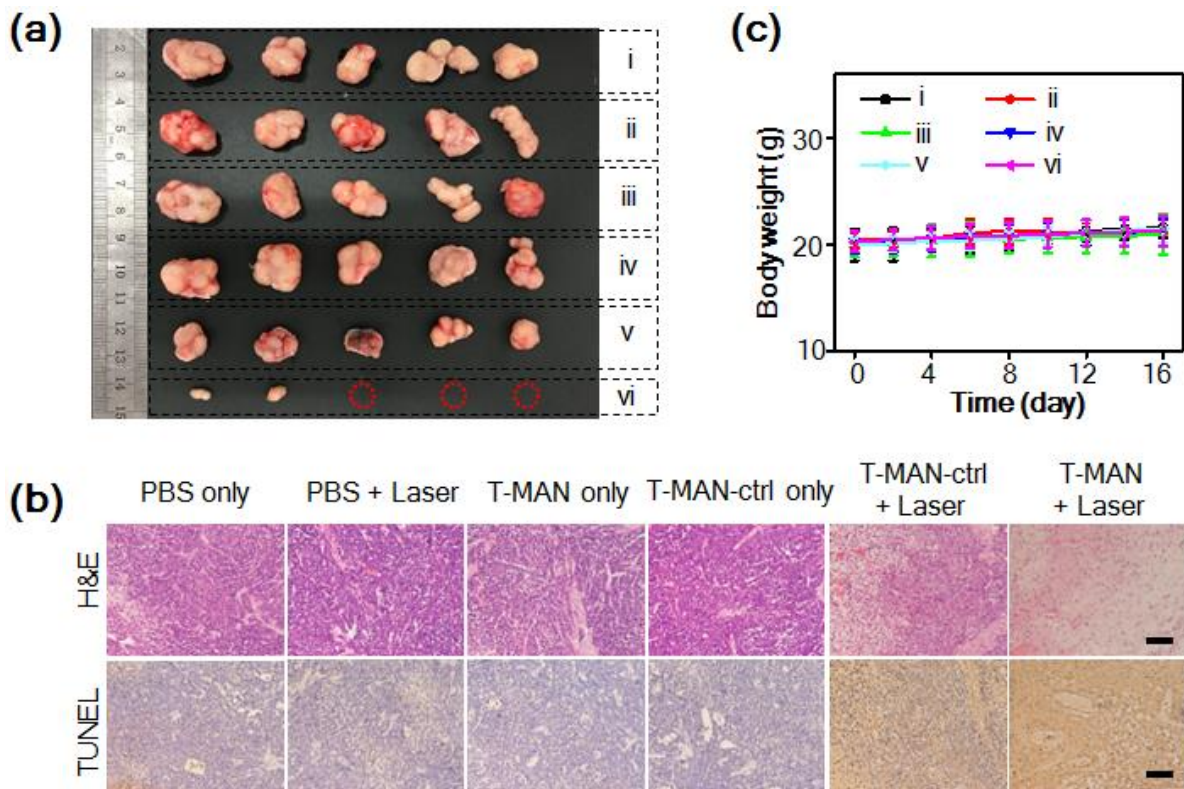


Figure S26. (a) Photographs of tumors on day 16 following treatment with PBS only (i), PBS plus laser irradiation (ii), T-MAN (iii), T-MAN-ctrl only (iv), T-MAN-ctrl plus laser irradiation (v) or T-MAN plus laser irradiation (vi). (b) H&E (up) and TUNEL staining (bottom) of tumor tissue slices resected from mice 1 day after treatment with PBS only, PBS plus laser irradiation, T-MAN, T-MAN-ctrl only, T-MAN-ctrl plus laser irradiation or T-MAN plus laser irradiation. Scale bars: 100 μ m. (c) Average body weight of mice after indicated treatments (n = 5).

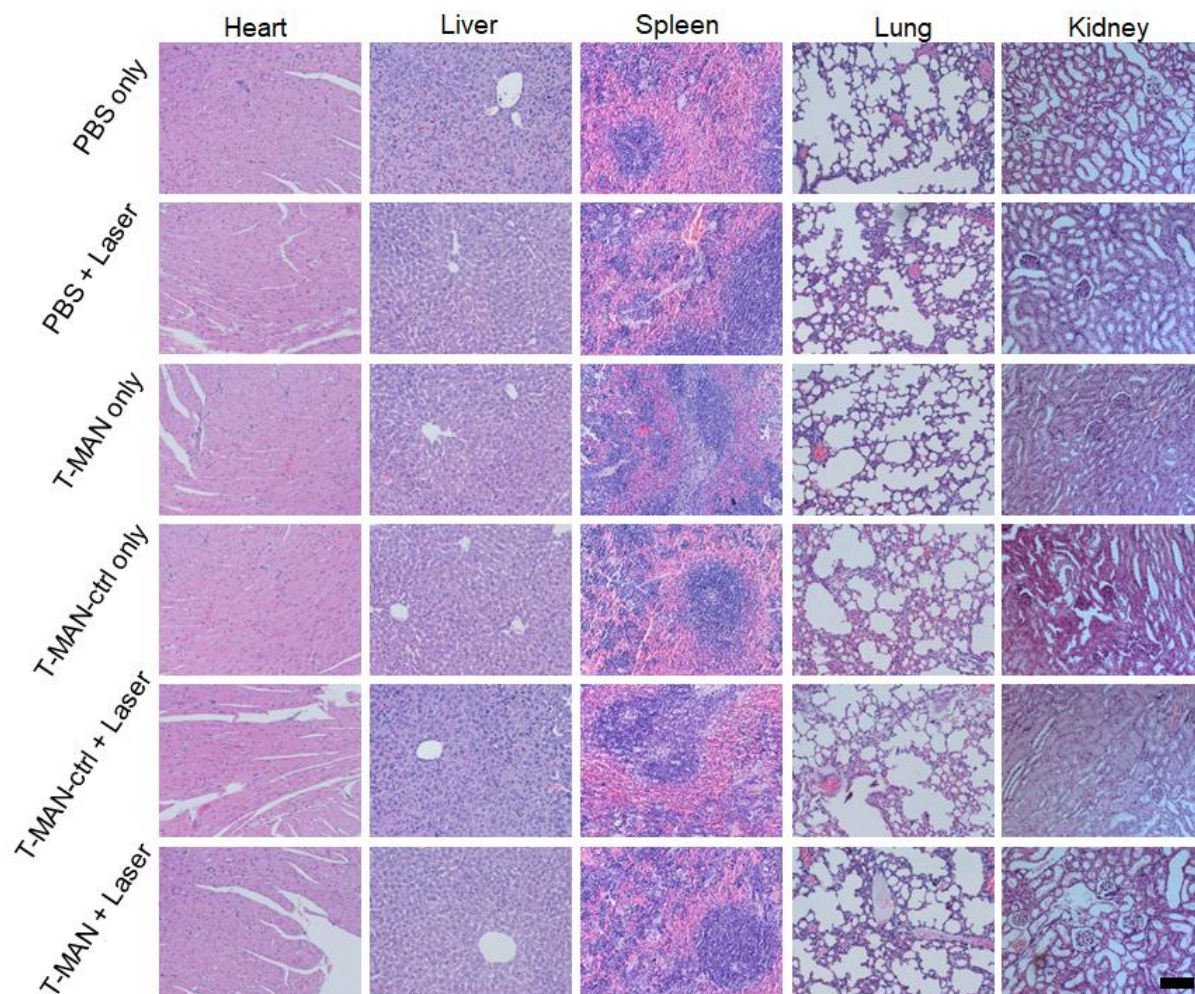


Figure S27. Representative H&E staining images of major organs including heart, liver, spleen, lung, kidneys resected from mice 12 h post indicated treatments. No obvious damage or lesion in these main organs was observed in T-MAN treated mice, suggesting that T-MAN had negligible *in vivo* side toxicity. Scale bar: 100 μ m.

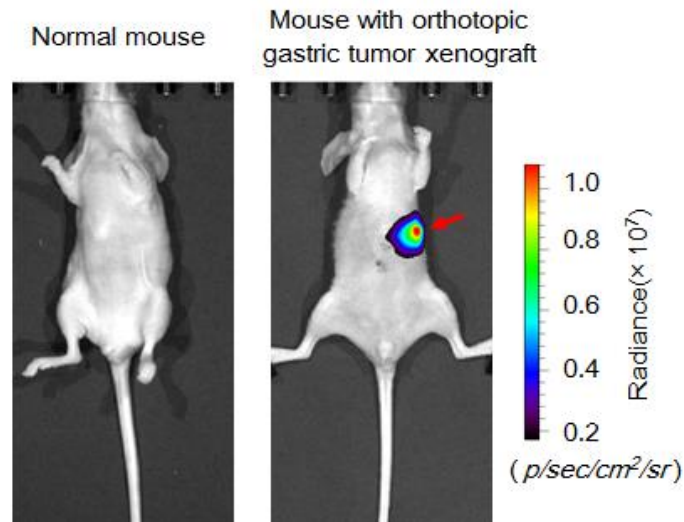


Figure S28. BL imaging of the stomachs in normal mouse or mouse with orthotopic MKN45/Luc gastric tumor formed by inoculation of MKN45/Luc cells into subserosal layer of the gastric wall for 2 weeks. The BL images were acquired in living mice following i.p. injection of ^{125}I -luciferin. Red arrow points to the orthotopic gastric tumor area. Strong BL was observed in mouse with inoculation of MKN45/Luc cells, but not in normal mouse, indicating that the orthotopic MKN45/Luc tumor was successfully formed in the stomach.

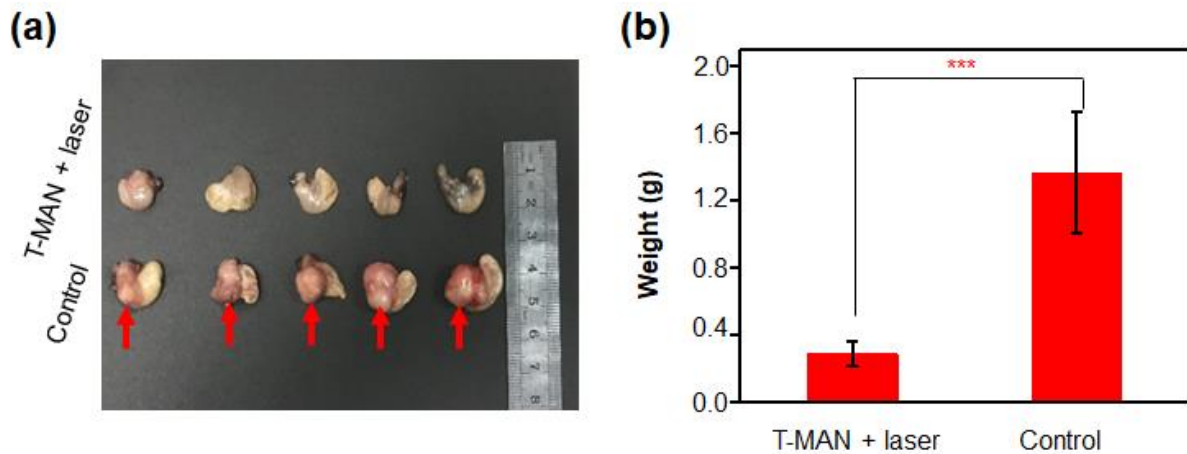


Figure S29. (a) Photograph and (b) average weight of dissected stomach organs of orthotopic MKN45/Luc tumor-bearing mice in treated group (T-MAN + laser) versus untreated group (Control). Red arrows point to the orthotopic gastric tumor tissues. Values were mean \pm SD ($n = 5$). *** $p < 0.001$. The results indicated that the orthotopic MKN45/Luc tumors were efficiently ablated in mice following PTT with T-MAN + laser irradiation.

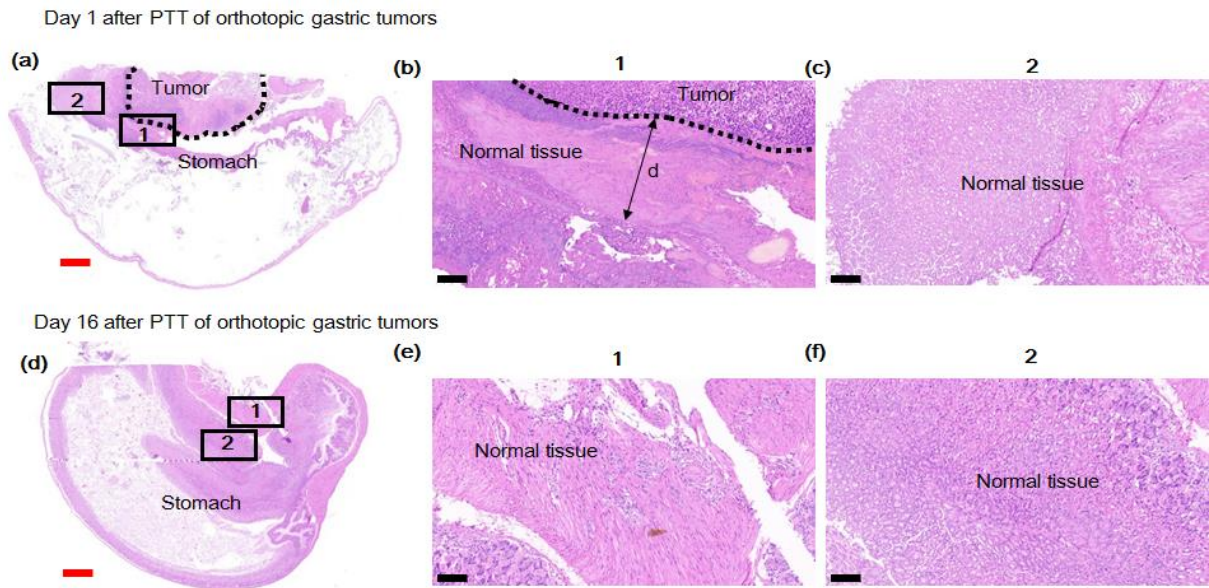


Figure S30. (a) Micrographs of H&E stained gastric tissue with orthotopic tumors at 1 day after PTT with T-MAN and 808 nm laser irradiation (0.85 W/cm^2 , 10 min). The dotted line indicated the margins of tumor tissue. (b,c) Enlarged micrographs as indicated by solid boxes 1 and 2 in (a). Black arrow indicates the damage stomach tissues with maximum distance of $360 \mu\text{m}$ from the margin of tumor tissues. (d) Micrographs of H&E stained gastric tissue with orthotopic tumors at 16 day after PTT. (e,f) Enlarged micrographs as indicated by solid boxes 1 and 2 in (d). Red scale bars: 1 mm. Black scale bars: $100 \mu\text{m}$.

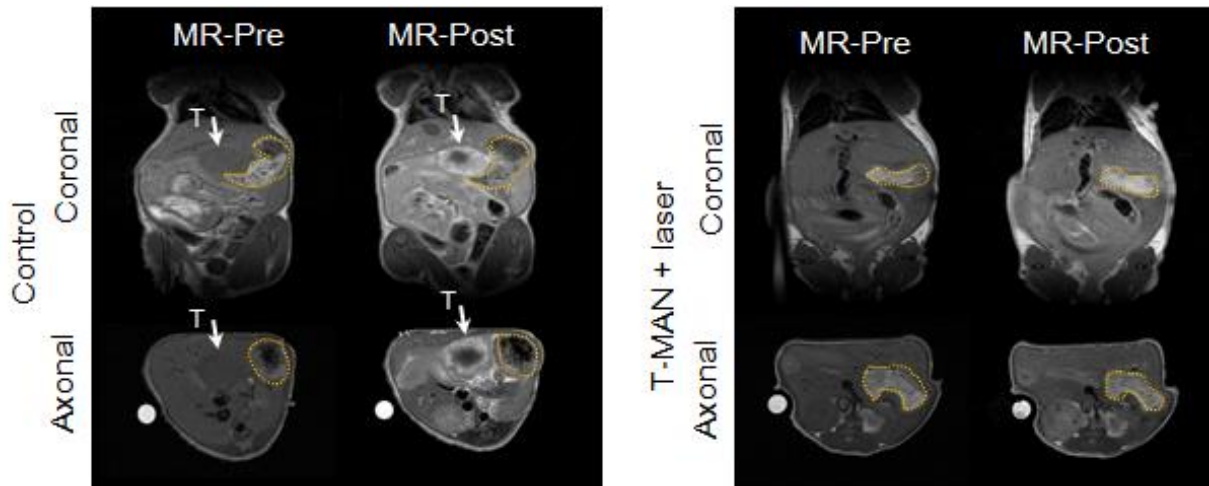


Figure S31. Noninvasive monitoring of therapeutic effect against orthotopic MKN45/Luc gastric tumors using T-MAN. T_1 -weighted MR images (1 T) of orthotopic MKN45/Luc gastric tumor-bearing mice on day 16 after treatment without (control) or with T-MAN and 808 nm laser irradiation (T-MAN + laser). White arrows indicate the location of orthotopic gastric tumors in untreated mice (Control), and yellow dashed circles indicate the locations of stomachs.

The images showed that the MR contrast in control group was significantly enhanced 12 h post i.v. injection of T-MAN, while in T-MAN and laser-treated group, the tumor tissue was hardly observed in mouse. These results suggested that the tumors in the stomach were efficiently ablated in mice upon PTT with T-MAN and laser irradiation, which were consistent to that observed from BL imaging. As such, T-MAN was also feasible for noninvasive monitoring of therapeutic effect against orthotopic gastric tumors *in vivo*.

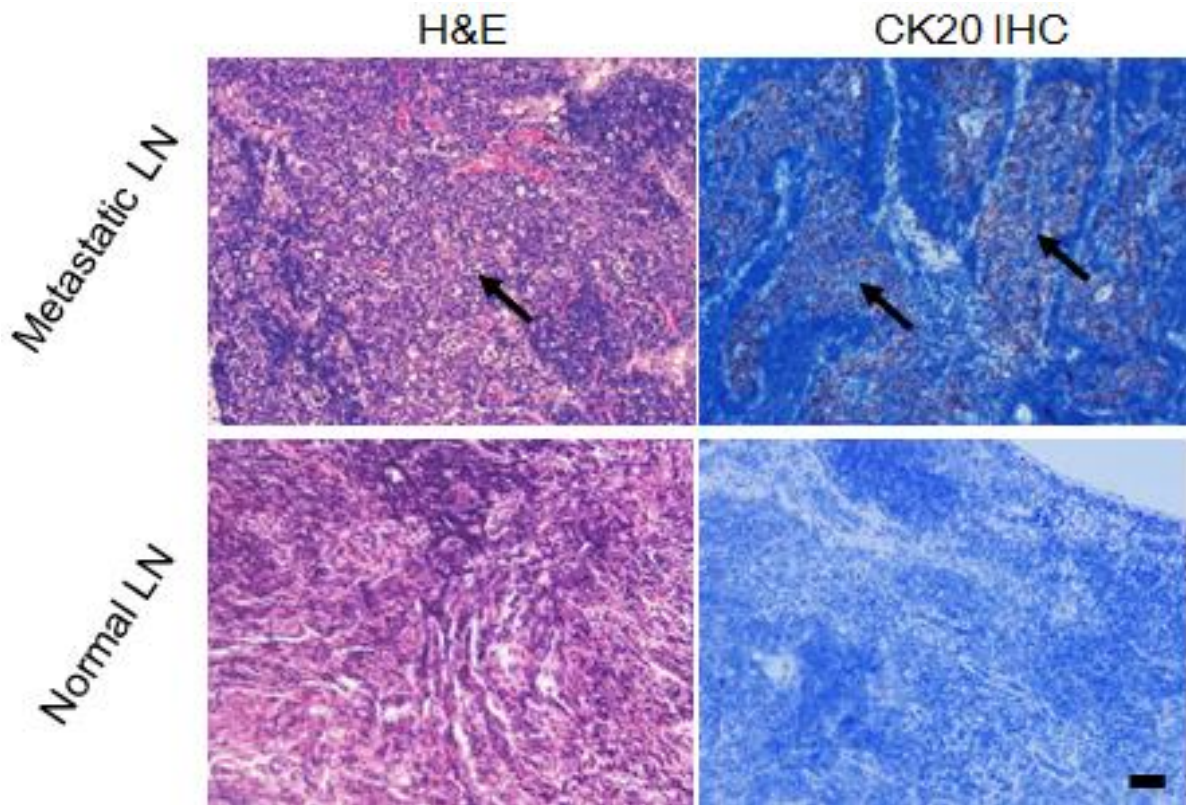


Figure S32. H&E and CK20 immunohistochemical staining of LN tissue slices resected from normal mice (normal LN) and mice with inoculation of the MKN45 cells on the right paw for three weeks. Black arrows point to the metastatic nodules in the lymph nodes. Scale bar: 50 μ m.

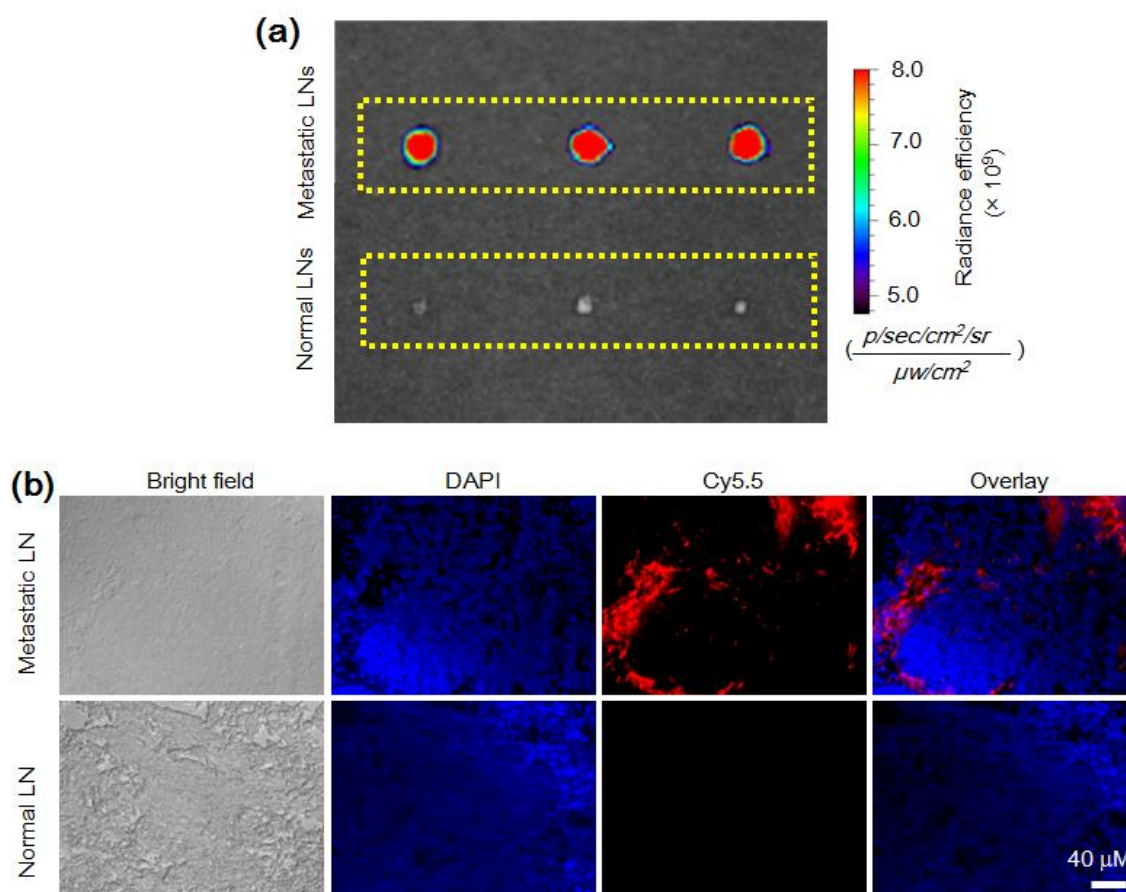


Figure S33. (a) *Ex vivo* FL imaging of metastatic and normal LNs, and (b) tissue slices resected from mice following s.c. injection of T-MAN into right leg. The LNs were resected from mice at 2 h after injection of T-MAN. The tissues were co-stained with DAPI.

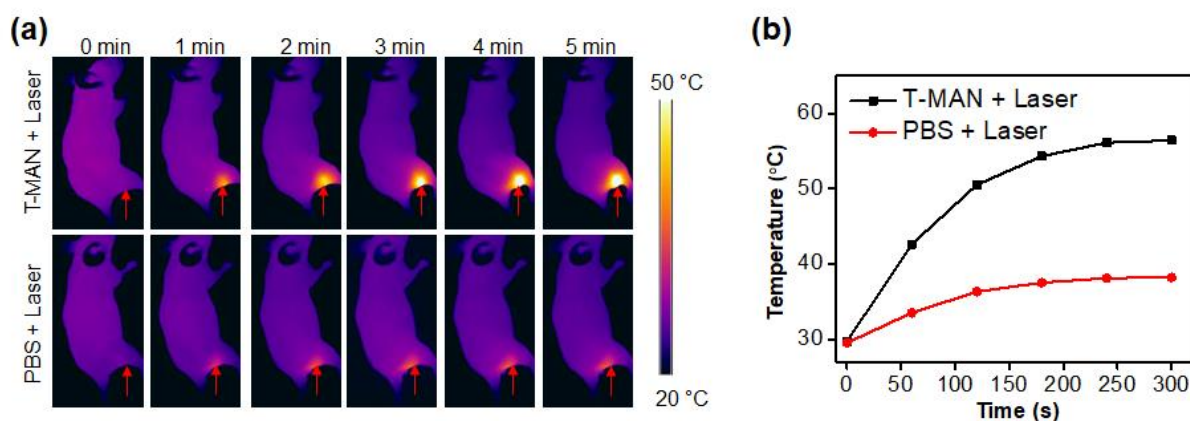


Figure S34. (a) Longitudinal IR thermal images and (b) the temperature changes of metastatic LN in living mice treated with T-MAN (2.5 mg/Kg Cu^{2+}) or PBS under 808 nm laser irradiation (0.5 W/cm^2) for 5 min.

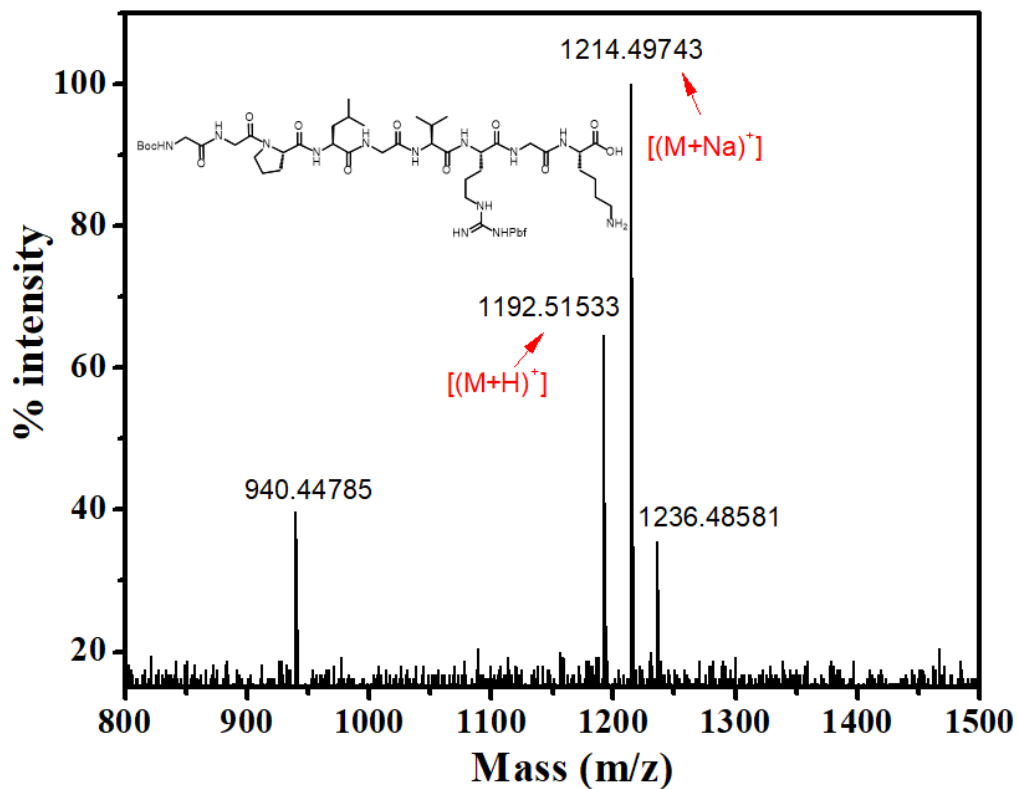


Figure S35. High-resolution MALDI-MS analysis of (Boc)GGPLGVR(Pbf)GK-OH.

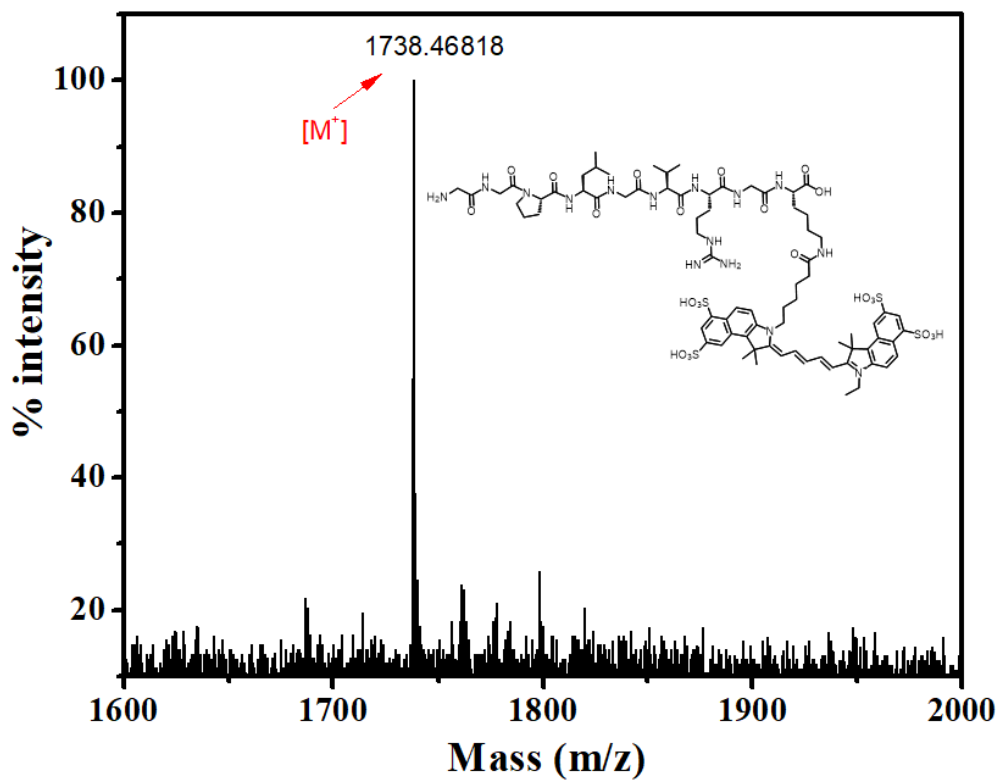


Figure S36. High-resolution MALDI-MS analysis of GGPLGVRGK(Cy5.5)-OH.

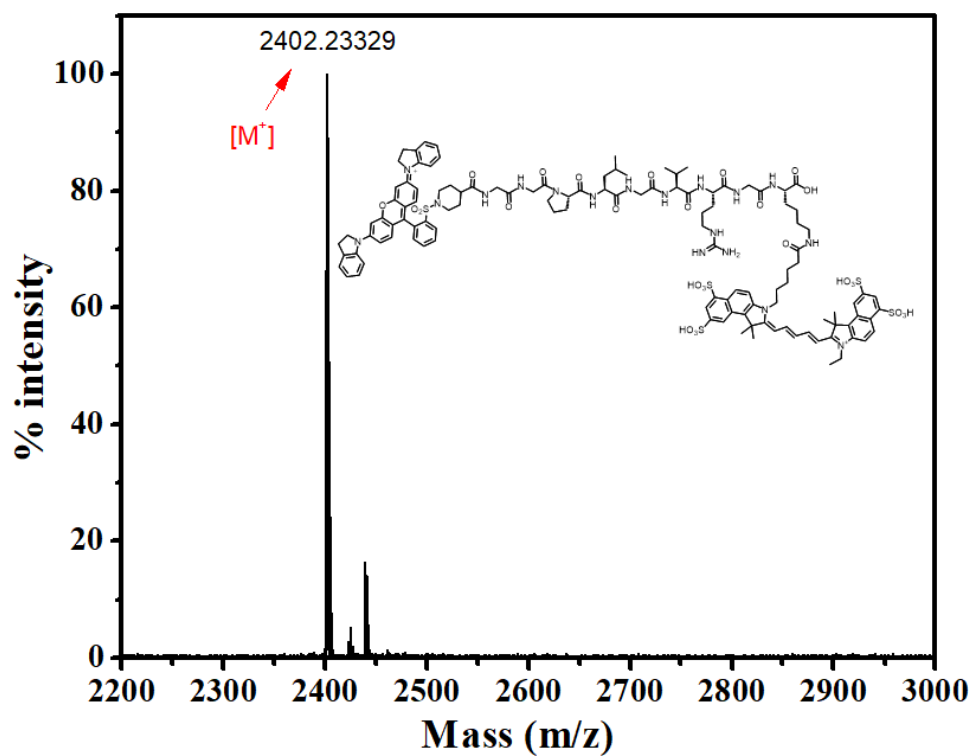


Figure S37. High-resolution MALDI-MS analysis of (QSY21)-GGPLGVRGK(Cy5.5)-OH.

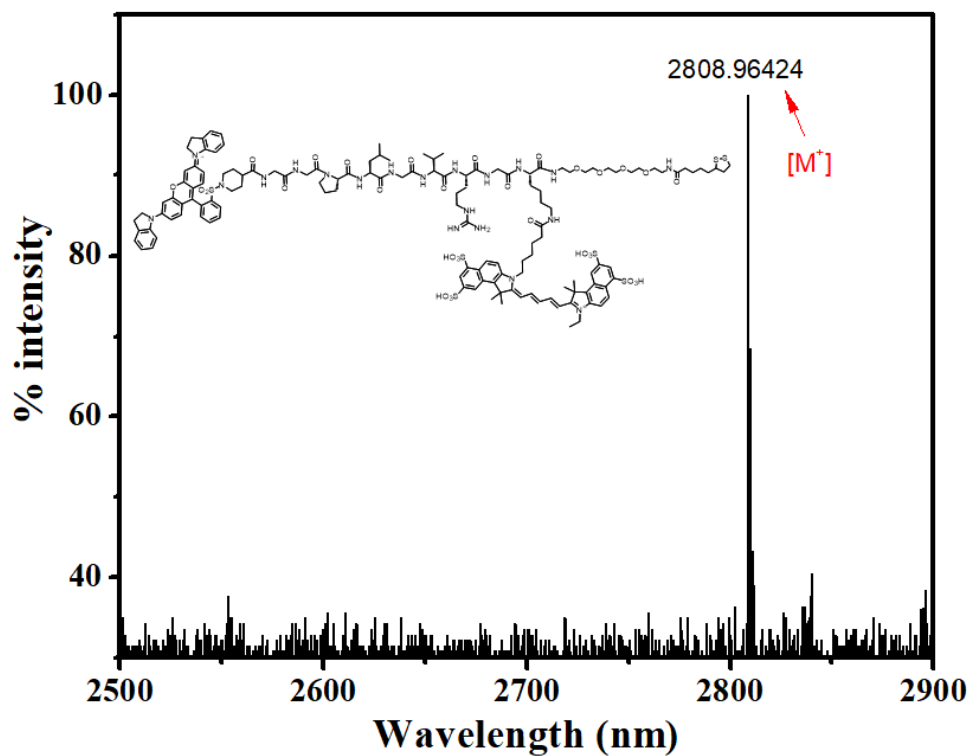


Figure S38. High-resolution MALDI-MS analysis of (QSY21)-GGPLGVRGK(Cy5.5)-SS.

Table S1. Summary of the reported MMP-2-activatable fluorescent probes.

Probe	λ_{ex} (nm)	λ_{em} (nm)	LOD	K_m (μM)	K_{cat} (s^{-1})	K_{cat}/K_m $\text{M}^{-1} \text{s}^{-1}$	Ref.
UCP-Peptide-CNP	980	547	2.46 fM ^b	N.D. ^a	N.D. ^a	N.D. ^a	7
PMPD-peptide-FITC	480	518	32 pM	N.D. ^a	N.D. ^a	N.D. ^a	8
GO-Pep-FITC	480	521	35 pM	N.D. ^a	N.D. ^a	N.D. ^a	9
Coumarin-peptide-Dabcyl	445	480	0.71 pM ^b	N.D. ^a	N.D. ^a	N.D. ^a	10
biotin-pep-BHQ-1	400	585	15 pM	N.D. ^a	N.D. ^a	N.D. ^a	11
5FAM ₃ -THP	480	510	N.D. ^a	8.7	0.092	1.1×10^4	12
5FAM ₆ -THP	480	510	N.D. ^a	4.3	0.065	1.5×10^4	12
M2AFPs	646	667	N.D. ^a	N.D. ^a	N.D. ^a	1.0×10^4	13
NiFe ₂ O ₄ MMP-2 responsive nanoprobe	328	393	N.D. ^a	6.56	9.8×10^{-5}	14.9	14
Cypate3-THP	780	810	N.D. ^a	8.19	0.056	0.68×10^4	15
Cypate3-(PEG)2-THP	780	810	N.D. ^a	10.9	0.099	0.91×10^4	15
fTHP	780	810	N.D. ^a	4.4	0.061	1.4×10^4	15
UCNP@p-Au	980	540	0.0056 fM ^b	400	28	7×10^4	16
GO-peptide-QXL	400	560	28.4 pM ^b	0.76	N.D. ^a	N.D. ^a	17
Probe 3a	N.D. ^a	N.D. ^a	$\sim 0.5 \text{ nM}$	62.5	3.9	6.3×10^4	18
LS276-THP	780	810	N.D. ^a	2.2	0.066	3×10^4	19
GO-P1 assembly	400	560	28.4 pM ^b	0.072	0.00083	1.1×10^4	20
T-MAN	670	690	0.64 pM	1.67	0.12	7.1×10^4	Our work

^a Not Determined.^b The number was calculated from the data in the reference: $C \text{ (mol/L)} = C \text{ (g/L)} / 71 \text{ kDa}$.**Table S2.** Comparison of the photothermal conversion efficiency between reported CuS nanoparticles and T-MAN.

CuS nanoparticles	Photothermal conversion efficiency	Ref.
Cu _{7.2} S ₄	56.7% (980 nm) ^a	21
Cu-Ag ₂ S/PVP	58.2% (808 nm) ^a	22
Cu ₂ MnS ₂	49.4% (1064 nm) ^a	23
Gd:CuS@BSA	32.3% (980 nm) ^a	24
CuS-PTX/SiO ₂	31.2% (980 nm) ^a	25
CuS-Fn	47.0% (808 nm) ^a	26
HCuS@Cu ₂ S@Au	35% (808 nm) ^a	27
CuS	50% (980 nm) ^a	28
Cu ₉ S ₅	25.7% (980 nm) ^a	29
CuS@mSiO ₂ -PEG	29.5% (980 nm) ^a	30
CuS	71.4% (806 nm) ^a	31
T-MAN	70.1% (808 nm) ^a	Our work

^a The numbers in brackets indicate the wavelength of laser used.

Note S1: Determination of the encapsulation efficiency

To evaluate the encapsulation efficiency, the amount of Gd/CuS nanodisks encapsulated in the Gd/CuS@DSPE micelles were determined by ICP-MS analysis, with the concentration of Cu^{2+} found to be 46.6 $\mu\text{g/mL}$. The concentration of Cu^{2+} in the Gd/CuS nanodisks input was ~48.9 $\mu\text{g/mL}$. Therefore, the encapsulation efficiency (EE%) was then calculated using the following equations:

$$\begin{aligned} \text{EE}\% &= \frac{\text{Amount of Cu}^{2+} \text{ in Gd/CuS@DSPE micelles}}{\text{Amount of Cu}^{2+} \text{ in Gd/CuS nanodisks input}} \times 100\% \\ &= \frac{C_{\text{Cu}^{2+} \text{ in Gd/CuS@DSPE micelles}} \times V_{\text{Gd/CuS@DSPE micelles}}}{C_{\text{Cu}^{2+} \text{ in Gd/CuS nanodisks input}} \times V_{\text{Gd/CuS nanodisks}}} \times 100\% \\ &= \frac{46.6 \text{ ug/mL} \times 10 \text{ mL}}{48.9 \text{ ug/mL} \times 10 \text{ mL}} \times 100\% = \sim 95.3\% \end{aligned}$$

Accordingly, the encapsulation efficiency (EE%) was calculated to be about ~95.3%.

Note S2: Evaluation of the number of cRGD and (QSY)-GGPLGVRGK(Cy5.5) on T-MAN.

(1) To evaluate the number of cRGD per T-MAN, we first quantified the amount of cRGD that was conjugated to the surface of total nanoparticles using HPLC assay. We added 0.1 mg of cRGD in total to modify the nanoparticles, and after reaction, the unconjugated cRGD was separated by ultrafiltration (amicon centrifugal filters, 10 kDa cutoff, 4000 rpm). The amount of cRGD in the filtrate was then analyzed by HPLC, showing that there was ~ 0.076 mg of cRGD in the filtrate on the basis of the standard curve. Thus, the amount of cRGD conjugated to the nanoparticles was calculated to be:

$$0.1 - 0.076 \text{ mg} = 0.024 \text{ mg} = 3.54 \times 10^{-8} \text{ mol.}$$

So the upload rate of cRGD could be calculated to be: $0.024 \text{ mg} / 0.1 \text{ mg} \times 100\% = 24\%$

Second, we measured the number of synthesized nanoparticles using the instrument of ViewSizer® 3000 (MANTA Instrument, Inc. America), and the results showed that the number was found to be $\sim 1.52 \pm 0.62 \times 10^{14}$ ($n = 5$).

Alternately, the number of T-MAN could also be estimated based on Cu element concentration:

According to the TEM images, Gd/CuS nanodisks showed a hexagonal structure with an average size of ~ 13 nm in diameter (d) and ~ 3 nm in thickness (h). The average volume of a single Gd/CuS nanodisk was calculated to be:

$$\begin{aligned} V_{\text{Gd/CuS nanodisk}} &= 6S_{tri} \times h = 6 \times \left(\frac{1}{2} \times \frac{13 \times 10^{-7} \text{ cm}}{2} \times \frac{13\sqrt{3} \times 10^{-7} \text{ cm}}{4} \right) \times 3 \times 10^{-7} \text{ cm} \\ &= 1.10 \times 10^{-19} \text{ cm}^3 \end{aligned}$$

Assumed that the synthesized Gd/CuS nanodisks had the same density of that of reported covellite CuS nanoparticles (4.6 g/cm^3)³², the mass of a single Gd/CuS nanodisk was estimated to be:

$$\begin{aligned} m_{\text{Gd/CuS nanodisk}} &= V_{\text{Gd/CuS nanodisk}} \times \rho_{\text{Gd/CuS nanodisk}} \\ &= 1.10 \times 10^{-19} \text{ cm}^3 \times 4.6 \text{ g} \cdot \text{cm}^{-3} = 5.06 \times 10^{-19} \text{ g} \end{aligned}$$

According to TEM images, the number (N) of Gd/CuS nanodisk encapsulated in each T-MAN nanoparticle was estimated to be 13 ± 3 ; the weight of Gd/CuS nanodisks in a single T-MAN nanoparticle was estimated to be:

$$\begin{aligned} m_{\text{Gd/CuS nanodisk per T-MAN}} &= m_{\text{Gd/CuS nanodisk}} \times N \\ &= 5.06 \times 10^{-19} \text{ g} \times (13 \pm 3) = (6.44 \pm 1.36) \times 10^{-18} \text{ g} \end{aligned}$$

The weight of Cu element in Gd/CuS in a single T-MAN nanoparticle was calculated to be:

$$\begin{aligned} m_{\text{Cu per T-MAN}} &= m_{\text{Gd/CuS nanodisk per T-MAN}} \times \frac{M_{\text{Cu}}}{M_{\text{Gd/CuS nanodisk}} (0.17/1.33)} \\ &= (6.44 \pm 1.36) \times 10^{-18} \text{ g} \times \frac{63.546}{157.25 \times 0.17 + 63.546 + 32.065 \times 1.33} \\ &= (3.08 \pm 0.65) \times 10^{-18} \text{ g} \end{aligned}$$

According to the ICP-MS analysis, the concentration of Cu^{2+} in solution (1 mL) was found to be $500 \mu\text{g/mL}$; therefore, the number ($N_{\text{T-MAN}}$) of T-MAN nanoparticles in solution was estimated to be:

$$N_{T-MAN} = \frac{m_{Cu} \text{ in the solution}}{m_{Cu} \text{ per T - MAN}} = \frac{500 \times 10^{-6} \text{ g} \cdot \text{mL}^{-1} \times 1 \text{ mL}}{(3.08 \pm 0.65) \times 10^{-18} \text{ g}} \\ = (1.69 \pm 0.33) \times 10^{14}$$

It was found that the number was similar to that measured by ViewSizer® 3000 ($\sim 1.52 \pm 0.62 \times 10^{14}$).

Accordingly, the number of cRGD per T-MAN nanoparticles could be estimated by the following formulas:

$$N_{cRGD} \text{ per T - MAN} = \frac{N_{cRGD}}{N_{T-MAN}} = \frac{3.54 \times 10^{-8} (\text{mol}) \times (6.02 \times 10^{23})}{(1.52 \pm 0.62) \times 10^{14}} = 140 \pm 46$$

Where N_{cRGD} stands for the total number of molecules binding to the total nanoparticles, N_{T-MAN} stands for the total number of nanoparticles.

The number of cRGD per T-MAN nanoparticle was calculated to be 140 ± 46 .

(2) To evaluate the number of (QSY)-GGPLGVRGK(Cy5.5) per T-MAN nanoparticle, we first measured the UV absorbance of (QSY)-GGPLGVRGK(Cy5.5) at 675 nm in the diluted nanoparticle solution (12.5-fold diluted, Figure 1d), which was found to be 0.376. As the extinction coefficient of (QSY)-GGPLGVRGK(Cy5.5) at 675 nm was $\sim 2.796 \times 10^5 \text{ M}^{-1} \text{ cm}^{-1}$, the concentration of Cy5.5 in 1 mL diluted solution could be calculated using the following formulas:

$$C_{(QSY)-GGPLGVRGK(Cy5.5)} = \frac{A_{675}}{\epsilon} = \frac{0.376}{2.796 \times 10^5 \text{ mol/L}} = 1.345 \times 10^{-6} \text{ mol/L}$$

Therefore, the amount of (QSY)-GGPLGVRGK(Cy5.5) in the stock solution of T-MAN was found to be: $1.345 \times 10^{-6} \text{ mol/L} \times 12.5 \times 1 \text{ mL} = 1.68 \times 10^{-5} \text{ mol/L} = 0.0168 \text{ } \mu\text{mol}$.

As the input amount was $0.061 \text{ } \mu\text{mol}$, the upload efficiency was calculated to be: $0.0168 \text{ } \mu\text{mol} / 0.061 \text{ } \mu\text{mol} \times 100 \% = 27.5 \%$

Based on the amount of (QSY)-GGPLGVRGK(Cy5.5) and the number of T-MAN nanoparticle, the (QSY)-GGPLGVRGK(Cy5.5) per T-MAN nanoparticle could be estimated by the following formulas:

$$N_{(QSY)-GGPLGVRGK(Cy5.5)} \text{ per T - MAN} \\ = \frac{N_{(QSY)-GGPLGVRGK(Cy5.5)}}{N_{T-MAN}} = \frac{0.0168 \mu\text{mol} \times (6.02 \times 10^{23})}{(1.52 \pm 0.62) \times 10^{14}} = 67 \pm 22$$

Where $N_{(QSY)-GGPLGVRGK(Cy5.5)}$ stands for the total number of (QSY)-GGPLGVRGK(Cy5.5) on the nanoparticle, and N_{T-MAN} stands for the total number of nanoparticles in the stock solution.

Accordingly, the $N_{(QSY)-GGPLGVRGK(Cy5.5)}$ of (QSY)-GGPLGVRGK(Cy5.5) per T-MAN was calculated to be about 67 ± 22 .

(3) To evaluate the number of Cu^{2+} and Gd^{3+} per T-MAN nanoparticle, we first measured the concentration of Cu^{2+} and Gd^{3+} in T-MAN nanoparticle solution by ICP-MS analysis, which was found to be 500 $\mu\text{g/mL}$ and 187.97 $\mu\text{g/mL}$. Therefore, the amount of Cu^{2+} and Gd^{3+} in the solution of T-MAN (1 mL) was found to be: 7.87 μmol and 1.20 μmol .

Based on the amount of Cu^{2+} and Gd^{3+} and the number of T-MAN nanoparticle, the Cu^{2+} and Gd^{3+} per T-MAN nanoparticle could be estimated by the following formulas:

$$N_{\text{Cu}^{2+}} \text{ per T - MAN} = \frac{N_{\text{Cu}^{2+}}}{N_{T-MAN}} = \frac{7.87 \mu\text{mol} \times (6.02 \times 10^{23})}{(1.52 \pm 0.62) \times 10^{14}} = (3.12 \pm 1.02) \times 10^4$$

$$N_{\text{Gd}^{3+}} \text{ per T - MAN} = \frac{N_{\text{Gd}^{3+}}}{N_{T-MAN}} = \frac{1.20 \mu\text{mol} \times (6.02 \times 10^{23})}{(1.52 \pm 0.62) \times 10^{14}} = (4.74 \pm 1.55) \times 10^3$$

Where $N_{\text{Cu}^{2+}}$ stands for the total number of Cu^{2+} on the nanoparticle, and $N_{\text{Gd}^{3+}}$ stands for the total number of Gd^{3+} on the nanoparticle.

Accordingly, the N of Cu^{2+} per T-MAN was calculated to be $(3.12 \pm 1.02) \times 10^4$, and the N of Gd^{3+} per T-MAN was calculated to be $(4.74 \pm 1.55) \times 10^3$.

Note S3: Evaluation of photothermal conversion efficiency of T-MAN.

Photothermal conversion efficiency (η) is a measure of how efficient a nanoparticle is in converting absorbed light into a temperature increase of its surroundings. The η value can be calculated as follows:

$$\eta = \frac{hS(T_{\max} - T_{\text{surr}}) - Q_{\text{dis}}}{I(1 - 10^{-A\lambda})} \times 100\%$$

where h is the heat transfer coefficient. A is the surface area of the sample well. T_{\max} of the equilibrium temperature in Figure S14a is 65.6 °C. T_0 of the ambient temperature is 28.1 °C. Q_{dis} is the heat energy of the quartz cell and solvent without nanoparticles, which is measured independently to be 4.6 mW. I of the laser power is 0.8 W/cm². A_{808} of the absorption intensity of T-MAN at 808 nm is 0.62, and η is the photothermal conversion efficiency.

The thermal time constant should be the same for either heating or cooling of the solution. hS can be determined by applying the linear time data from the cooling period vs Ln (θ):

$$hS = \frac{m \cdot C_{H_2O}}{\tau_s}$$

where the mass of the sample solution (m) is 0.2 g, and its heat capacity value (C_{H_2O}) is approximated to be 4.2 J g⁻¹ K⁻¹. The slope of the linear equation (τ_s) in Figure S13b is 72.78 s.

$$hS = \frac{0.2 \times 4.2}{72.78} = 0.0115$$

Finally, substituting hS value into Equation, η can be calculated as following:

$$\eta = \frac{0.0115 \times (65.6 - 28.1) - 0.0046}{0.8 \times (1 - 10^{-0.62})} \times 100\% = \frac{0.4266}{0.6081} \times 100\% = 70.1\%$$

Reference:

- (1) Zhang, H.; Zhang, Y.; Yu, J.; Yang, D. *J. Phys. Chem. C* **2008**, *112*, 13390-13394.
- (2) Busuttil, R. A.; Liu, D. S.; Costanzo, N. D.; Schröder, J.; Mitchell, C.; Boussioutas, A. *Sci. Rep.* **2018**, *8*, 825.
- (3) Sun, F.; Yu, M.; Yu, J.; Liu, Z.; Zhou, X.; Liu, Y.; Ge, X.; Gao, H.; Li, M.; Jiang, X. *Cell Death Dis.* **2018**, *9*, 52.
- (4) Shi, H.; Yan, R.; Wu, L.; Sun, Y.; Liu, S.; Zhou, Z.; He, J.; Ye, D. *Acta Biomater.* **2018**, *72*, 256-265.
- (5) Huo, D.; He, J.; Li, H.; Huang, A. J.; Zhao, H. Y.; Ding, Y.; Zhou, Z. Y.; Hu, Y. *Biomaterials* **2014**, *35*, 9155-9166.
- (6) Chen, Q.; Liang, C.; Sun, X.; Chen, J.; Yang, Z.; Zhao, H.; Feng, L.; Liu, Z. *Proc. Natl. Acad. Sci. U. S. A.* **2017**, *114*, 5343-5348.
- (7) Wang, Y.; Shen, P.; Li, C.; Wang, Y.; Liu, Z. *Anal. Chem.* **2012**, *84*, 1466-1473.
- (8) Wang, Z.; Li, X.; Feng, D.; Li, L.; Shi, W.; Ma, H. *Anal. Chem.* **2014**, *86*, 7719-7725.
- (9) Song, E.; Cheng, D.; Song, Y.; Jiang, M.; Yu, J.; Wang, Y. *Biosens. Bioelectron.* **2013**, *47*, 445-450.
- (10) He, G.; Yang, L.; Qian, X.; Li, J.; Yuan, Z.; Li, C. *Int. J. Mol. Med.* **2017**, *39*, 1571-1579.
- (11) Pillai, S. S.; Yukawa, H.; Onoshima, D.; Biju, V.; Baba, Y. *Anal. Sci.* **2017**, *33*, 137-142.
- (12) Zhang, X.; Bresee, J.; Cheney, P. P.; Xu, B. G.; Bhowmick, M.; Cudic, M.; Fields, G. B.; Edwards, W. B. *Molecules* **2014**, *19*, 8571-8588.
- (13) Lebel, R.; Bonin, M. A.; Zriba, R.; Radulska, A.; Neugebauer, W.; Lepage, M. *Contrast Media Mol. Imaging* **2012**, *7*, 328-337.
- (14) Sun, L.; Xie, S.; Ji, X.; Zhang, J.; Wang, D.; Lee, S. J.; Lee, H.; He, H.; Yang, V. *Biomater. Sci.* **2018**, DOI: 10.1039/C8BM00593A.
- (15) Zhang, X.; Bresee, J.; Fields, G. B.; Edwards, W. B. *Molecules* **2014**, *24*, 3786-3790.
- (16) Chan, Y. C.; Chen, C. W.; Chan, M. H.; Chang, Y. C.; Chang, W. M.; Chi, L. H.; Yu, H. M.; Lin, Y. F.; Tsai, D. P.; Liu, R. S. *Biosens. Bioelectron.* **2016**, *80*, 131-139.
- (17) Kwak, S. Y.; Yang, J. K.; Jeon, S. J.; Kim, H. I.; Yim, J.; Kang, H.; Kyeong, S.; Lee, Y. S.; Kim, J. H. *Adv. Funct. Mater.* **2015**, *24*, 5119-5128.
- (18) Matsuo, K.; Kamada, R.; Mizusawa, K.; Imai, H.; Takayama, Y.; Narazaki, M.; Matsuda, T.; Takaoka, Y.; Hamachi, I. *Chem. Eur. J.* **2014**, *19*, 12875-12883.
- (19) Akers, W. J.; Xu, B.; Lee, H.; Sudlow, G. P.; Fields, G. B.; Achilefu, S.; Edwards, W. B. *Bioconjugate Chem.* **2012**, *23*, 656-663.

- (20) Yang, J. K.; Kwak, S. Y.; Jeon, S. J.; Lee, E.; Ju, J. M.; Kim, H. I.; Lee, Y. S.; Kim, J. H. *Nanoscale* **2016**, *8*, 12272-12281.
- (21) Li, B.; Wang, Q.; Zou, R.; Liu, X.; Xu, K.; Li, W.; Hu, J. *Nanoscale* **2014**, *6*, 3274-3282.
- (22) Dong, L.; Ji, G.; Liu, Y.; Xu, X.; Lei, P.; Du, K.; Song, S.; Feng, J.; Zhang, H. *Nanoscale* **2017**, *10*, 825-831.
- (23) Ke, K.; Yang, W.; Xie, X.; Liu, R.; Wang, L. L.; Lin, W. W.; Huang, G.; Lu, C. H.; Yang, H. H. *Theranostics* **2017**, *7*, 4763-4776.
- (24) Yang, W.; Guo, W.; Le, W.; Lv, G.; Zhang, F.; Lei, S.; Wang, X.; Wang, J.; Sheng, W.; Jin, C. *ACS Nano* **2016**, *10*, 10245-10257.
- (25) He, J.; Ai, L.; Liu, X.; Huang, H.; Li, Y.; Zhang, M.; Zhao, Q.; Wang, X.; Chen, W.; Gu, H. *J. Mat. Chem. B* **2018**, *6*, 1035-1043..
- (26) Wang, Z.; Huang, P.; Jacobson, O.; Wang, Z.; Liu, Y.; Lin, L.; Lin, J.; Lu, N.; Zhang, H.; Tian, R. *ACS Nano* **2016**, *10*, 3453-3460.
- (27) Deng, X.; Li, K.; Cai, X.; Liu, B.; Wei, Y.; Deng, K.; Xie, Z.; Wu, Z.; Ma, P.; Hou, Z. *Adv. Mater.* **2017**, *29*, 1701266.
- (28) Tian, Q.; Tang, M.; Sun, Y.; Zou, R.; Chen, Z.; Zhu, M.; Yang, S.; Wang, J.; Wang, J.; Hu, J. *Adv. Mater.* **2011**, *23*, 3542-3547.
- (29) Tian, Q.; Jiang, F.; Zou, R.; Liu, Q.; Chen, Z.; Zhu, M.; Yang, S.; Wang, J.; Wang, J.; Hu, J. *ACS Nano* **2011**, *5*, 9761-9771.
- (30) Liu, X. J.; Ren, Q. L.; Fu, F. F.; Zou, R. J.; Wang, Q.; Xin, G. B.; Xiao, Z. Y.; Huang, X. J.; Liu, Q.; Hu, J. Q. *Dalton T.* **2015**, *44*, 10343-10351.
- (31) Marin, R.; Skripka, A.; Besteiro, L. V.; Benayas, A.; Wang, Z.; Govorov, A. O.; Canton, P.; Vetrone, F. *Small* **2018**, *14*, e1803282.
- (32) Raevskaya, A. E.; Stroyuk, A. L.; Kuchmii, S. Y.; Kryukov, A. I. *J. Mol. Catal. A-Chem.* **2004**, *212*, 259-265.